Exploring the dust content of galactic winds with *Herschel* – II. Nearby dwarf galaxies

Alexander McCormick,[1][*] Sylvain Veilleux,[2][*] Marcio Meléndez,[3,4] Crystal L. Martin,[5] Joss Bland-Hawthorn,[6] Gerald Cecil,[7] Fabian Heitsch,[7] Thomas Müller,[8] David S. N. Rupke[9] and Chad Engelbracht[10]

[1]*Department of Physics, University of South Florida, Tampa, FL 33620, USA*
[2]*Department of Astronomy and Joint Space-Science Institute, University of Maryland, College Park, MD 20742, USA*
[3]*NASA Goddard Space Flight Center, Greenbelt, MD 20771, USA*
[4]*Wyle Science, Technology and Engineering Group, 1290 Hercules Avenue, Houston, TX 77058, USA*
[5]*Department of Physics, University of California, Santa Barbara, CA 93106, USA*
[6]*Department of Physics, University of Sydney, Sydney, NSW 2006, Australia*
[7]*Department of Physics, University of North Carolina, Chapel Hill, NC 27599, USA*
[8]*Max-Planck-Institute for Extraterrestrial Physics (MPE), Giessenbachstrasse 1, D-85748 Garching, Germany*
[9]*Department of Physics, Rhodes College, Memphis, TN 38112, USA*
[10]*Department of Astronomy, University of Arizona, Tucson, AZ 85721, USA (Deceased)*

ABSTRACT

We present the results from an analysis of deep *Herschel Space Observatory* observations of six nearby dwarf galaxies known to host galactic-scale winds. The superior far-infrared sensitivity and angular resolution of *Herschel* have allowed detection of cold circumgalactic dust features beyond the stellar components of the host galaxies traced by *Spitzer* 4.5 μm images. Comparisons of these cold dust features with ancillary data reveal an imperfect spatial correlation with the ionized gas and warm dust wind components. We find that typically ∼10–20 per cent of the total dust mass in these galaxies resides outside of their stellar discs, but this fraction reaches ∼60 per cent in the case of NGC 1569. This galaxy also has the largest metallicity (O/H) deficit in our sample for its stellar mass. Overall, the small number of objects in our sample precludes drawing strong conclusions on the origin of the circumgalactic dust. We detect no statistically significant trends with star formation properties of the host galaxies, as might be expected if the dust were lifted above the disc by energy inputs from ongoing star formation activity. Although a case for dust entrained in a galactic wind is seen in NGC 1569, in all cases, we cannot rule out the possibility that some of the circumgalactic dust might be associated instead with gas accreted or removed from the disc by recent galaxy interaction events, or that it is part of the outer gas-rich portion of the disc that lies below the sensitivity limit of the *Spitzer* 4.5 μm data.

Key words: galaxies: dwarf – galaxies: general – galaxies: haloes – galaxies: interactions – galaxies: star formation – galaxies: structure.

1 INTRODUCTION

Galactic winds driven by stellar processes and active galactic nuclei (AGNs) are a fundamental mechanism of galaxy evolution (see Veilleux, Cecil & Bland-Hawthorn 2005, for a review). Simulations have shown that the outflows of material in winds can inhibit the growth of central supermassive black holes and curb the star formation rates (SFRs) in galaxies (e.g. Naab & Ostriker 2017, and references therein). Winds have also been invoked to explain a host of galaxy observations, including the mass–metallicity relation (e.g. Tremonti et al. 2004; Mannucci et al. 2010; Lara-López et al. 2010; Kashino et al. 2016; Telford et al. 2016; Barrera-Ballesteros et al. 2017; Sánchez et al. 2017) and the relation between the central black hole mass and the bulge velocity dispersion (e.g. Ferrarese & Merritt 2000; Gebhardt et al. 2000; Gültekin et al. 2009; Kormendy & Ho 2013). Furthermore, the ubiquity of galactic winds at $z > 1$ (e.g. Weiner et al. 2009; Steidel et al. 2010; Shapley 2011;

Erb et al. 2012; Martin et al. 2012, and references therein) points to their importance in understanding the past history of the universe. Therefore, detailed observations of galactic winds are critical to fleshing out the narrative of galaxy evolution. Although negative feedback almost certainly asserts greater influence at high redshift, where strong starbursts and AGNs are more commonplace, nearby sources provide the best opportunities for detailed observations of the galactic winds. Dwarf galaxies are particularly important in this context since their evolution is highly sensitive to the effects of galactic winds and feedback in general (e.g. Vogelsberger et al. 2014; Muratov et al. 2015; Schaye et al. 2015; Davé et al. 2017).

Prior to 2005, much of the observational data on galactic winds emphasized the entrained ionized material (e.g. Heckman, Armus & Miley 1990; Lehnert & Heckman 1995; Veilleux et al. 2005), the neutral gas (e.g. Heckman et al. 2000; Rupke, Veilleux & Sanders 2002, 2005a,b, 2005c; Schwartz & Martin 2004; Martin 2005), and the highly ionized X-ray emitting plasma (e.g. Read, Ponman & Strickland 1997; Martin 1999; Pietsch et al. 2000; Martin, Kobulnicky & Heckman 2002; McDowell et al. 2003; Ehle et al. 2004; Huo et al. 2004; Strickland et al. 2004a,b). Only a few observations showed evidence that these outflows also entrained dust (e.g. Alton, Davies & Bianchi 1999; Heckman et al. 2000; Radovich, Kahanpää & Lemke 2001; Tacconi-Garman et al. 2005) and molecular gas (e.g. Curran et al. 1998; Walter, Weiss & Scoville 2002). This state of affairs has changed dramatically in recent years, largely driven by the new capabilities of space-borne infrared observatories (e.g. Engelbracht et al. 2006; Kaneda et al. 2009; Fischer et al. 2010; Kaneda et al. 2010; Roussel et al. 2010; Sturm et al. 2011; McCormick, Veilleux & Rupke 2013; Veilleux et al. 2013; Meléndez et al. 2015) and ground-based near-infrared imagers and spectrometers and millimetre (mm)-wave interferometers (e.g. Sakamoto et al. 2006; Veilleux, Rupke & Swaters 2009; Feruglio et al. 2010; Irwin et al. 2011; Alatalo et al. 2011; Aalto et al. 2012; Bolatto et al. 2013; Rupke & Veilleux 2013b; Cicone et al. 2014; Alatalo 2015; Feruglio et al. 2015; Lindberg et al. 2016; Veilleux et al. 2017). These new results have in turn triggered a flurry of theoretical studies and numerical simulations of the interaction of winds with the denser interstellar medium (ISM) aimed at understanding the nature and impact of these dusty neutral and molecular outflows on galaxy evolution (e.g. Cooper et al. 2008, 2009; Faucher-Giguère & Quataert 2012; Zubovas et al. 2013; Zubovas & King 2014; McCourt et al. 2015; Nims, Quataert & Faucher-Giguère 2015; Scannapieco & Bruggen 2015; Ferrara & Scannapieco 2016; Brüggen & Scannapieco 2016; Banda-Barragán et al. 2016; Tanner, Cecil & Heitsch 2016, 2017; Richings & Faucher-Giguere 2018).

Dust grains found in the ISM were formed in the atmospheres of evolved stars or during the outbursts of novae and supernovae, but can also be destroyed and reconstituted in the ISM. Interstellar dust plays a crucial role in galaxy evolution and star formation. It absorbs and scatters light, it can act as the catalyst to form molecules through reactions not possible in the gas phase, it can enrich or deplete the interstellar gas via destruction and evaporation of grains or condensation on grains, and electrons liberated from dust grains via the photoelectric effect can heat the ISM gas (Krügel 2002; Lequeux 2005). Therefore, investigating the distribution, mass, and energy of the dust in wind galaxies provides critical information for understanding galaxy evolution. Observations of dusty winds may even catch galaxies in the act of expelling their star formation fuel, eventually halting stellar nurseries.

In the first paper of this series (Meléndez et al. 2015, hereafter Paper I), we presented *Herschel Space Observatory* (Pilbratt et al. 2010) observations of the nearby wind galaxy NGC 4631. In this second paper of the series, we examine six nearby dwarf galaxies selected to host known galactic winds. The new results are based on an analysis of our deep observations of these objects with *Herschel*. The angular resolution and sensitivity of these data, far superior to previous far-infrared (FIR) data obtained with *Spitzer* Multiband Imaging Photometer (MIPS), allow us to detect and characterize cool dust that lies outside the extent of the stellar component of the host galaxy (hereafter called 'circumgalactic dust').

In Section 2, we describe our sample, the methods of acquisition of the *Herschel* data, and the ancillary data. In Sections 3 and 4, we explain the process used to reduce the *Herschel* data and our analysis of these data, respectively. We present our results of this analysis in Section 5, including maps of each galaxy in *Herschel's* 70, 160, 250, 350, and 500 μm channels, and comparisons of the basic properties of the circumgalactic dust with those of the host galaxies. Our results are summarized in Section 6. Appendix A contains a short discussion of each galaxy.

2 SAMPLE AND DESCRIPTION OF THE DATA

The six nearby dwarf galaxies in our sample were selected based on their proximity (less than ∼10 Mpc), their stellar masses (less than ∼10^{10} M$_\odot$), and on previous evidence of galactic winds at other wavelengths. Table 1 lists the galaxies, some of their properties, and selected references to evidence of galactic winds for each source. This sample is not homogeneous – it spans a broad range of properties. All of these galaxies are actively forming stars but one of them, He 2–10, likely also hosts an AGN (Reines et al. 2011, 2016). He 2–10 is represented with an open circle in some of the figures to differentiate it from the galaxies hosting purely star formation. We also note that the membership of NGC 3077 in the M81 group complicates the interpretation of the circumgalactic material, so this object is also represented with a different symbol in the figures and is treated separately in the discussion of the results.

We acquired very deep (>6 h) *Herschel Space Observatory* PACS (Poglitsch et al. 2010) images in the 70 and 160 μm channels for each of the six objects in our sample as part of a two-cycle observational program to investigate the circumgalactic dust of nearby star-forming galaxies in general. The long exposure times for our very deep PACS images were necessary to detect the faint circumgalactic dust emission and distinguish it from point spread function (PSF) artefacts near the peak of the infrared spectral energy distribution (SED). Each of the 70 and 160 μm PACS observations consisted of a four times repeated scan map of either 30 or 40 scan legs 3 arcmin in length and separated by 4 arcsec to fully map the galaxies and to obtain a very high and homogeneous coverage well beyond the stellar extent of the galaxies. These two-band scan-map observations were conducted seven times, each time at a different angle with respect to the detector array orientation. This technique virtually eliminates systematic noise from low-level striping and reaches approximately Poisson noise limits. We also acquired SPIRE (Griffin et al. 2010) data at 250, 350, and 500 μm for the one galaxy in our sample which had not already been observed (NGC 1800) and downloaded the archived SPIRE data for the other five galaxies. The dominant source of noise in deep SPIRE data is confusion noise, i.e. confusion with unresolved foreground and background sources, which does not depend on exposure time. SPIRE reaches this confusion limit in exposure times of ∼0.6 h or less (it depends on the exact wavelength); hence the exposure times of the SPIRE data never exceed this limit. The SPIRE observations were performed in the LargeScanMap mode using orthogonal scan directions and multiple iterations for four

Table 1. Nearby dwarf galaxies and their properties.

Galaxy	Type	Morph.	D_{25} (arcmin)	d (Mpc)	Scale (pc arcsec^{-1})	L_{IR} ($10^9\,L_\odot$)	$12+$ log(O/H)	M_{HI} $10^8\,M_\odot$	M_{H_2} $10^8\,M_\odot$	$\log(M_*/M_\odot)$	SFR ($M_\odot\,yr^{-1}$)	Σ_{SFR} ($M_\odot\,yr^{-1}\,kpc^{-2}$)	Wind/eDIG Ref.
[1]	[2]	[3]	[4]	[5]	[6]	[7]	[8]	[9]	[10]	[11]	[12]	[13]	[14]
He 2-10	Hɪɪ + AGN	I0? pec	1.74	10.5	50.9	7.00	8.80	3.37	1.85	9.5†	0.81	0.23	1,2,3
NGC 1569	Hɪɪ	IBm	3.63	3.36	16.3	1.24	8.16	2.11	0.0262	9.14	0.23	0.037	4,5,6,7,8,9
NGC 1705	Hɪɪ	SA0⁻ pec	1.91	5.10	24.7	0.0617*	8.48	0.953	1.06	8.37†	0.053	0.0084	10,11,12,13
NGC 1800	Hɪɪ	IB(s)m	2.00	7.40	35.9	0.137*	8.58	1.58	0.670	8.84	0.034	0.022	8,14,15,16
NGC 3077	Hɪɪ	I0 pec	5.37	3.83	18.6	0.608	8.78	8.95	0.0541	9.44	0.077	0.093	8,17,18,19,20
NGC 5253	Hɪɪ	pec	5.01	3.77	18.3	1.48	8.28	1.50	0.0354	9.05†	0.23	0.44	13,21,22,23,24

Notes: – Column 1: Galaxy name. Column 2. Optical/ultraviolet spectral types are identified as either star-forming Hɪɪ region-like galaxies (Hɪɪ) or contaminated by an AGN (Hɪɪ + AGN). Column 3. de Vaucouleurs morphological type from de Vaucouleurs et al. (1991, , hereafter RC3). Column 4. Diameter (major axis) in arcminutes based on 25th magnitude *B*-band observations (RC3). Column 5. Redshift-independent distance. References: He 2–10: Tully 1988; NGC 1569: Grocholski et al. 2008; NGC 1705: Tosi et al. 2001; NGC 1800: Tully 1988: NGC 3077: Dalcanton et al. 2009; NGC 5253: Sakai et al. 2004. Column 6. Spatial scale assuming the redshift-independent distance listed in column (5). Column 7. Infrared luminosity (8–1000 μm) expressed in units of $10^9\,L_\odot$, determined by fitting a three component MBB to *Herschel* fluxes densities (this work), plus *Spitzer* and *IRAS* flux densities listed in the NED (Moshir et al. 1990; Sanders et al. 2003), and the distances listed in column (5). The * indicates that the determination of these L_{IR} values included some *IRAS* flux upper limits. Column 8. Metallicity derived using the method in Pettini & Pagel (2004) (O3N2), which has then been converted via the prescriptions in Kewley & Ellison (2008) to conform with the metallicities in Tremonti et al. (2004). Uncertainties in the metallicity come from a combination of the method used (∼0.1 dex) and the conversion (∼0.06 dex). A solar metallicity [12 + log(O/H)] = 8.69 is assumed (Allende Prieto et al. 2001). Emission-line strength references: He 2–10, NGC 1569, NGC 5253: Kobulnicky, Kennicutt & Pizagno 1999; NGC 1705: Moustakas et al. 2010; NGC 1800: Moustakas & Kennicutt 2006; NGC 3077: McQuade, Calzetti & Kinney 1995. Column 9. Neutral gas (Hɪ) masses based on values from the HIPASS (Koribalski et al. 2004) and THINGS (Walter et al. 2008) surveys and the distances listed in column (5). Column 10. Molecular (H$_2$) gas masses calculated from CO data from Young et al. (1995) (He 2–10, NGC 1569, NGC 3077, NGC 5253) using the method in Bolatto et al. (2013) (equations 3 and 7) or by multiplying the SFR by an assumed depletion time of 2 Gyr (NGC 1705 & NGC 1800). Column 11. Stellar masses calculated using the *M/L* derived from Bell et al. (2003), Two Micron All Sky Survey *K* magnitudes (Skrutskie et al. 2003), and optical colours (either $B - V$ or $B - R$). The † indicates masses adopted from Zastrow et al. (2013) calculated using this method. We used the optical colours listed in Kennicutt et al. (2009) (equation 16) to calculate the masses of NGC 1569, NGC 1800, and NGC 3077. Column 12. SFR from combining $L_{H\alpha}$ (Kennicutt et al. 2008) and L_{IR} (this work, see above) according to the prescription in Kennicutt et al. (2009) (equation 16). Column 13. SFR surface density using the SFR listed in column (12) and the ionized gas radius ($R_{H\alpha}$) listed in Calzetti et al. (2010). Column 14. Selected references to a galactic wind or extraplanar diffuse ionized gas (eDIG): (1) Méndez et al. (1999); (2) Johnson et al. (2000); (3) Kobulnicky, Smith & Gallagher (2008); (4) Waller (1991); (5) Hunter, Hawley & Gallagher (1993); (6) Heckman et al. (1995); (7) della Ceca et al. (1996); (8) Martin (1997); (9) Westmoquette, Smith & Gallagher (2008); (10) Meurer, Freeman & Dopita (1989); (11) Meurer et al. (1992); (12) Meurer, Staveley-Smith & Killeen (1998); (13) Heckman et al. (2001); (14) Marlowe et al. (1995); (15) Hunter (1996); (16) Rasmussen, Stevens & Ponman (2004); (17) Thronson, Wilton & Ksir (1991); (18) Martin (1998); (19) Ott, Martin & Walter (2003); (20) Calzetti et al. (2004); (21) Calzetti et al. (1999); (22) Strickland & Stevens (1999); (23) Kobulnicky & Stevens (1999); (24) Zastrow et al. (2011).

Table 2. *Herschel Space Observatory* data.

Galaxy	Instrument (PACS[c]/SPIRE)	t_{int} [a] (h)	OD/Obs. ID(s)[b]	Principal investigator (OT/KPGT/SDP/KPOT)[d]
He 2–10	PACS	6.56	1076/1342244883-89	Veilleux, S. (OT2)
	SPIRE	0.07	0374/1342196888	Madden, S. (KPGT)
NGC 1569	PACS	6.56	1058/1342243816-22	Veilleux, S. (OT2)
	SPIRE	0.15	0318/1342193013	Madden, S. (KPGT)
NGC 1705	PACS	6.56	0968/1342236656-62	Veilleux, S. (OT1)
	SPIRE	0.20	0158/1342186114	Madden, S. (SDP)
NGC 1800	PACS	6.56	1377/1342263895-901[e]	Veilleux, S. (OT2)
	SPIRE	0.16	1024/1342240035	Veilleux, S. (OT2)
NGC 3077	PACS	8.74	1059/1342243845-51	Veilleux, S. (OT2)
	SPIRE	0.58	0318/1342193015	Kennicutt, R. C., Jr. (KPOT)
NGC 5253	PACS	8.74	1194/1342249927-33	Veilleux, S. (OT2)
	SPIRE	0.29	0459/1342203078	Madden, S. (KPGT)

[a]Total integration time in hours of the observation.

[b]*Herschel* Operation Day/Observation ID number(s).

[c]The PACS photometer scan maps were either 3 arcmin scan legs × 30 legs × 4 arcsec leg separation (He 2–10, NGC 1569, NGC 1705, NGC 1800) or 3 arcmin scan legs × 40 legs × 4 arcsec leg separation (NGC 3077 and NGC 5253).

[d]*Herschel* Open Time (OT), Key Programme Guaranteed Time (KPGT), Science Demonstration Phase (SDP), or Key Programme Open Time (KPOT).

[e]The PACS photometer observations from OD1377 (NGC 1800) suffered from a detector problem: after OD 1375 half of the red PACS photometer array was lost. Point-source photometry was still possible, but with lower coverage. Given the small size of NGC 1800, this problem had no impact on the quality of the data.

out of the six galaxies (single iterations for He 2–10 and NGC 1569). The *Herschel* data are summarized in Table 2. The *Herschel* observations were performed between 2012 January and 2013 March.

In addition to the new *Herschel* data, we also brought together ancillary data for each galaxy in four additional bands: Hα, 4.5, 8.0, and 24 μm. The ancillary data are summarized in Table 3 and discussed in more detail below.

3 DATA REDUCTION

Once the *Herschel* observations were completed, we extracted the new PACS and SPIRE data from the Herschel Science Archive. We downloaded the archival *Spitzer* Infrared Array Camera (IRAC; 4.5 and 8.0 μm) and MIPS (24 μm) data from the NASA/IPAC Infrared Science Archive. Before performing any reduction, we briefly examined the new *Herschel* data with version 10.3.0 of the Herschel Interactive Processing Environment (HIPE; Ott 2010), and we also inspected the Hα data and pipeline-processed *Spitzer* data (PBCDs) using SAOImage DS9.

3.1 *Herschel* data reduction

Following the steps in Meléndez et al. (2015), we reprocessed our *Herschel* data with HIPE up to Level-1 employing the PACS photometer pipeline (Balog et al. 2014) and then passed these data on to the SCANAMORPHOS v21 software (Roussel 2013). Since our deep *Herschel* observations aimed to detect very faint emission from cold dust in circumgalactic regions, we employed SCANAMORPHOS, which was built specifically to handle scan mode observations like ours, the preferred acquisition mode for nearby galaxies. SCANAMORPHOS exploits the redundancy of the observations in order to subtract low-frequency noise due to thermal and non-thermal components. It also masks high-frequency artefacts like cosmic ray hits before projecting the data on to a map. The final pixel sizes, which are ∼1/4 the size of the PSFs for each detector, are 1.4, 2.85, 4.5, 6.25, and 9.0 arcsec for the 70, 160, 250, 350, and 500 μm maps, respec-

tively. The *Herschel* maps are shown in Figs 1(a)–(f) along with the ancillary Hα, 4.5, 8.0, and 24 μm data.

3.2 *Spitzer* data reduction

Our reduction of the *Spitzer* IRAC data followed the same procedures as those described in McCormick et al. (2013), summarized here. Starting from the basic calibrated data, we corrected any electronic and optical banding in the 8.0 μm channel. In several of our sample galaxies, the bright nuclei generate broad PSFs in both the 4.5 and 8.0 μm channels, which overlap with circumgalactic regions, so we subtracted the wings of any broad PSFs using the APEX and APEX QA modules of the *Spitzer Science Center* provided MOPEX software (Makovoz & Khan 2005) . The 4.5 μm IRAC channel provides a better representation of the stellar emission than the 3.6 μm IRAC channel, since polycyclic aromatic hydrocarbon (PAH) emission from star formation in the galaxy discs may contaminate the 3.6 μm IRAC channel – see fig. 1 in Reach et al. (2006). Where necessary, we also performed a background subtraction to better distinguish background flux from circumgalactic features. Once the basic calibrated data were processed, we created maps of both channels using MOPEX. For NGC 1569, NGC 1705, and NGC 5253, we used the previously reduced data presented in McCormick et al. (2013).

4 DATA ANALYSIS

4.1 Disc–circumgalactic decomposition

Differentiating between a galaxy and its circumgalactic or extraplanar or halo region necessitates defining an edge or border between the two components when analysing an image projected on the sky. This process is necessarily subjective since the transition between the host galaxy and its halo is smooth and gradual. It is particularly important to keep this in mind when dealing with dwarf galaxies, since they often have H I discs or structures that extend beyond their stellar components (e.g. Ashley et al. 2014). Here, we defined an

Table 3. Ancillary data.

Galaxy	Band	t_{int}^a (s)	Observatory/Instrument	Obs. ID(s)[b]	PI(s)[c]
He 2–10	Hα	1200	Magellan/MMTF	...	Oey, S.
	4.5 μm	41.6	*Spitzer*/IRAC	4329472	Rieke, G.
	8.0 μm	41.6	*Spitzer*/IRAC	4329472	Rieke, G.
	24 μm	2.62	*Spitzer*/MIPS	4347904	Rieke, G.
NGC 1569	Hα	300	KPNO/Bok	...	Martin, C. L.
	4.5 μm	52	*Spitzer*/IRAC	4434944	Fazio, G.
	8.0 μm	52	*Spitzer*/IRAC	4434944	Fazio, G.
	24 μm	2.62	*Spitzer*/MIPS	4435456	Fazio, G.
NGC 1705	Hα	1200	Magellan/MMTF	...	Oey, S.
	4.5 μm	214.4	*Spitzer*/IRAC	5535744, 5536000	Kennicutt, R. C., Jr.
	8.0 μm	214.4	*Spitzer*/IRAC	5535744, 5536000	Kennicutt, R. C., Jr.
	24 μm	3.67	*Spitzer*/MIPS	5549312	Kennicutt, R. C., Jr.
NGC 1800	Hα	901.2	KPNO/Bok	...	Martin, C. L.
	4.5 μm	428.8	*Spitzer*/IRAC	22530304, 22530560, 22530816, 22531072	Kennicutt, R. C., Jr.
	8.0 μm	428.8	*Spitzer*/IRAC	22530304, 22530560, 22530816, 22531072	Kennicutt, R. C., Jr.
	24 μm	3.67	*Spitzer*/MIPS	22624000	Kennicutt, R. C., Jr.
NGC 3077	Hα	1000	KPNO/Bok	...	Kennicutt, R. C., Jr.
	4.5 μm	4758.4 (804)[d]	*Spitzer*/IRAC	4331520, 22000640, 22354944, 22357760, 22358016, 22539520, 22539776	Kennicutt, R. C., Jr., Neff, S., Rieke, G.
	8.0 μm	4758.4 (804)[d]	*Spitzer*/IRAC	4331520, 22000640, 22354944, 22357760, 22358016, 22539520, 22539776	Kennicutt, R. C., Jr., Neff, S., Rieke, G.
	24 μm	3.67	*Spitzer*/MIPS	17597696	Rieke, G.
NGC 5253	Hα	1200	Magellan/MMTF	...	Oey, S., Veilleux, S., Zastrow, J.
	4.5 μm	249.6	*Spitzer*/IRAC	4386048	Houck, J. R.
	8.0 μm	249.6	*Spitzer*/IRAC	4386048	Houck, J. R.
	24 μm	3.67	*Spitzer*/MIPS	22679040	Kennicutt, R. C., Jr.

[a]Total integration time in seconds.
[b]Observation ID number(s).
[c]Principal investigator(s).
[d]Total IRAC mosaic integration time for NGC 3077 (typical mosaic pixel integration time).

edge by choosing an isophote of 0.1 MJy sr⁻¹ in the predominantly stellar emission of the IRAC 4.5 μm channel map of each galaxy in our sample. This surface brightness threshold was selected to be faint enough to represent the outer boundary of the stellar emission, but sufficiently bright so that this boundary is not sensitive to the noise structure (this surface brightness threshold is greater than 4σ above the background noise for each map). This limit effectively corresponds to a uniform stellar mass surface density threshold across our sample. Using this method does not account for the potential occultation or coincidence of circumgalactic and disc emission due to inclination. However, any inclination effect will tend to reduce the amount of circumgalactic emission, not increase it. Therefore, we can consider these regions as setting an effective lower limit on the circumgalactic emission. For the sake of consistency and simplicity, we will call the regions encompassed within this 4.5 μm surface brightness threshold 'disc' regions, although most of the galaxies in our sample do not exhibit a classical disc morphology. The disc and circumgalactic regions defined in this fashion are shown in Figs 2(a)–(f). The circumgalactic flux region for NGC 1569 is necessarily conservative because of the proximity of Galactic cirrus emission which are noticeably impinging on the circumgalactic region in the SPIRE maps (see Figs 1b and 2b).

4.2 Removal of the disc PSFs with a CLEAN algorithm

In both the PACS and SPIRE instruments, the PSFs are broad enough that the wings from bright disc sources bleed out and contribute excess flux to the circumgalactic regions where we are looking for just the faint circumgalactic dust emission. To account for this excess, we employed a modified version of the CLEAN algorithm[1] (Högbom 1974). Our CLEAN algorithm finds the peak pixel within an area similar to the disc region, subtracts the appropriate PSF scaled by a pre-defined gain as a fraction of the peak pixel value, and repeats these two steps until the peak pixel value meets or drops below a pre-defined minimum threshold value. Once the minimum threshold value is reached, the algorithm outputs component and residual images. Since the galaxies in our sample contain broad, bright areas within their disc regions, we chose observations of Vesta (Obs. IDs 1342195624, 1342195625, also the reference PSF for PACS) and Uranus (Obs. ID 1342197342) as our beam PSFs. We selected *Herschel* observations of Vesta and Uranus with the same scan speed as our observations, which is important for matching the shape of the PSFs. We processed the Vesta and Uranus PSFs through the same combination of HIPE and SCANAMORPHOS as described in Section 3.1. Next, we rotated the PSFs to match the galaxy observations, centred the PSFs on their central pixels, and scaled the PSFs by normalizing their central peak pixels to a value of 1 for gain multiplication. Finally, we applied our CLEAN algorithm to each of the PACS and SPIRE images iteratively lowering the threshold value to determine circumgalactic flux value convergence. Fig. 3 illustrates the 'before' and 'after' results of applying our CLEAN algorithm to the maps of NGC 1569. Across all bands before application of the CLEAN algorithm, we find that ∼75 per cent (standard deviation
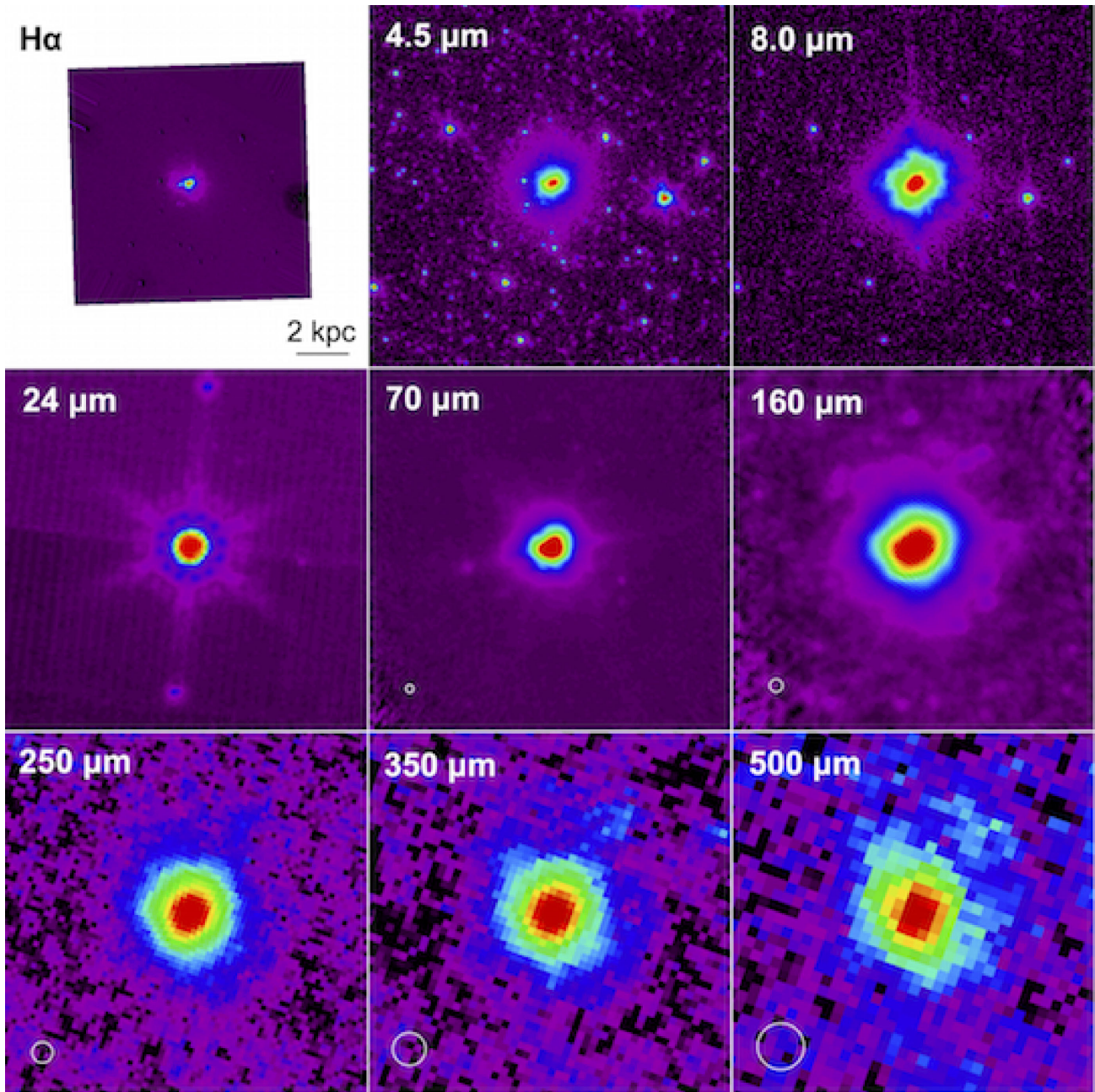
---

[1] Adapted from http://www.mrao.cam.ac.uk/~bn204/alma/python-clean.html.

Figure 1. (a) He 2–10 – Hα (Zastrow et al. 2013), IRAC 4.5 and 8.0 µm, and MIPS 24 µm (*Spitzer* archive, this work), PACS 70 and 160 µm, and SPIRE 250, 350, and 500 µm (this work). All images are displayed on a logarithmic intensity scale. North is up and east is to the left in all images. The bar in the Hα image indicates the scale in all images. The white circles in the 70, 160, 250, 350, and 500 µm panels indicate the full width at half-maximum of the PSF for each channel. (b) NGC 1569 – Hα (Martin 1997), IRAC 4.5 and 8.0 µm (McCormick et al. 2013), otherwise, the same as in (a). (c) NGC 1705 – Hα (Zastrow et al. 2013), IRAC 4.5 and 8.0 µm (McCormick et al. 2013), otherwise, the same as in (a). (d) NGC 1800 – Hα (Martin 1997), otherwise, the same as in (a). (e) NGC 3077 – Hα (Dale et al. 2009), otherwise, the same as in (a). (f) NGC 5253 – Hα (Zastrow et al. 2011), IRAC 4.5 and 8.0 µm (McCormick et al. 2013), otherwise, the same as in (a).

≈20 per cent) of the flux in the circumgalactic region has bled out from the disc region. There is no apparent trend with wavelength. Residual maps after application of our CLEAN algorithm are shown in Figs 2(a)–(f).

4.3 *Herschel* flux measurements

In each of the five *Herschel* bands, we took global flux measurements from the original SCANAMORPHOS maps using a circular or

elliptical aperture centred on the galaxy and containing the most extended circumgalactic cold dust features. Note that the most extended features did not always appear in the same *Herschel* band. In each of the five bands, we calculated the cleaned circumgalactic flux by adding up the flux in the CLEAN residual maps outside of the disc region out to the boundary of the region used for the global flux measurements. We then calculated the corrected disc flux by subtracting the cleaned circumgalactic flux from the original global flux value. Using this method, the excess flux that bled out of the
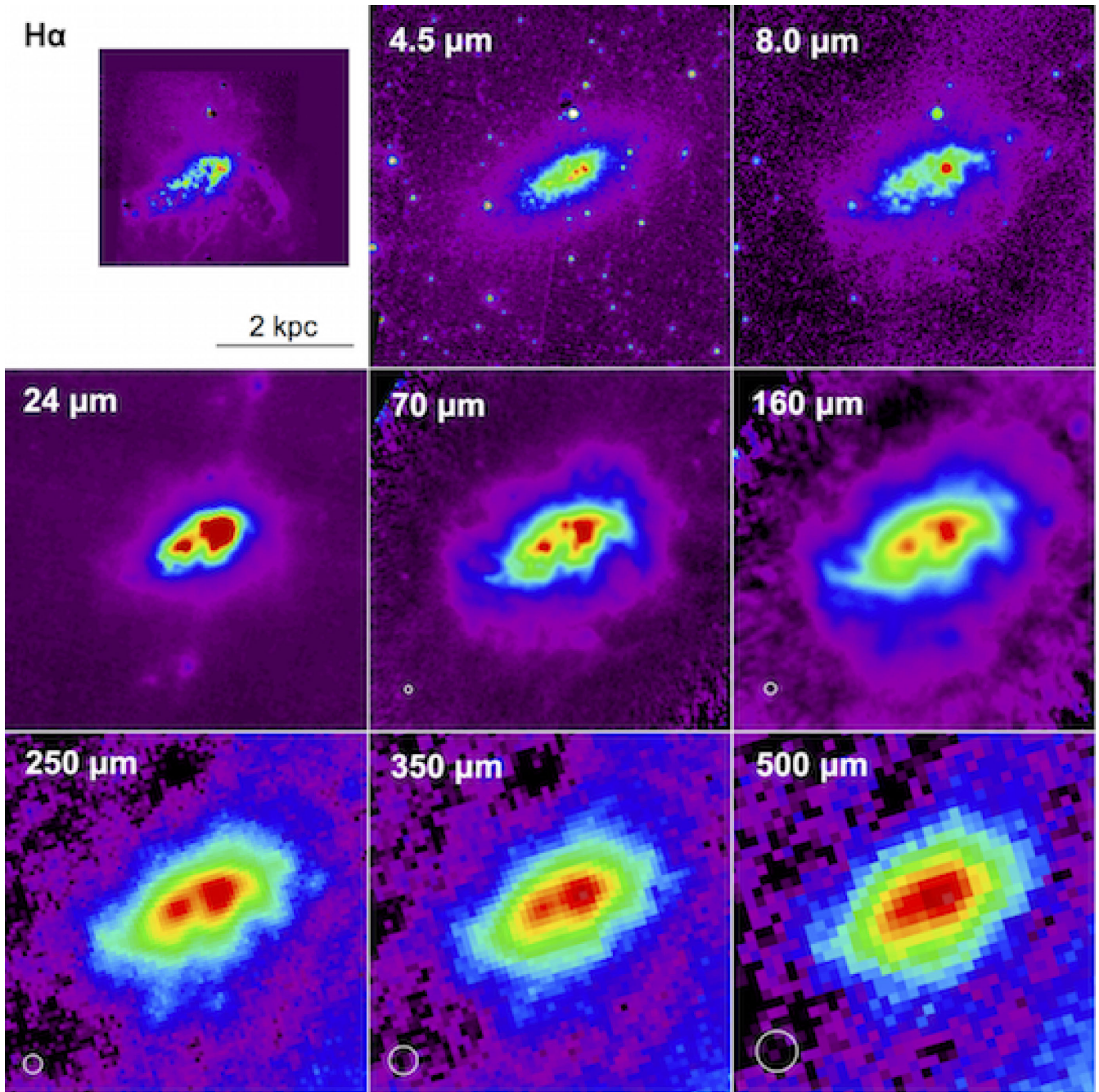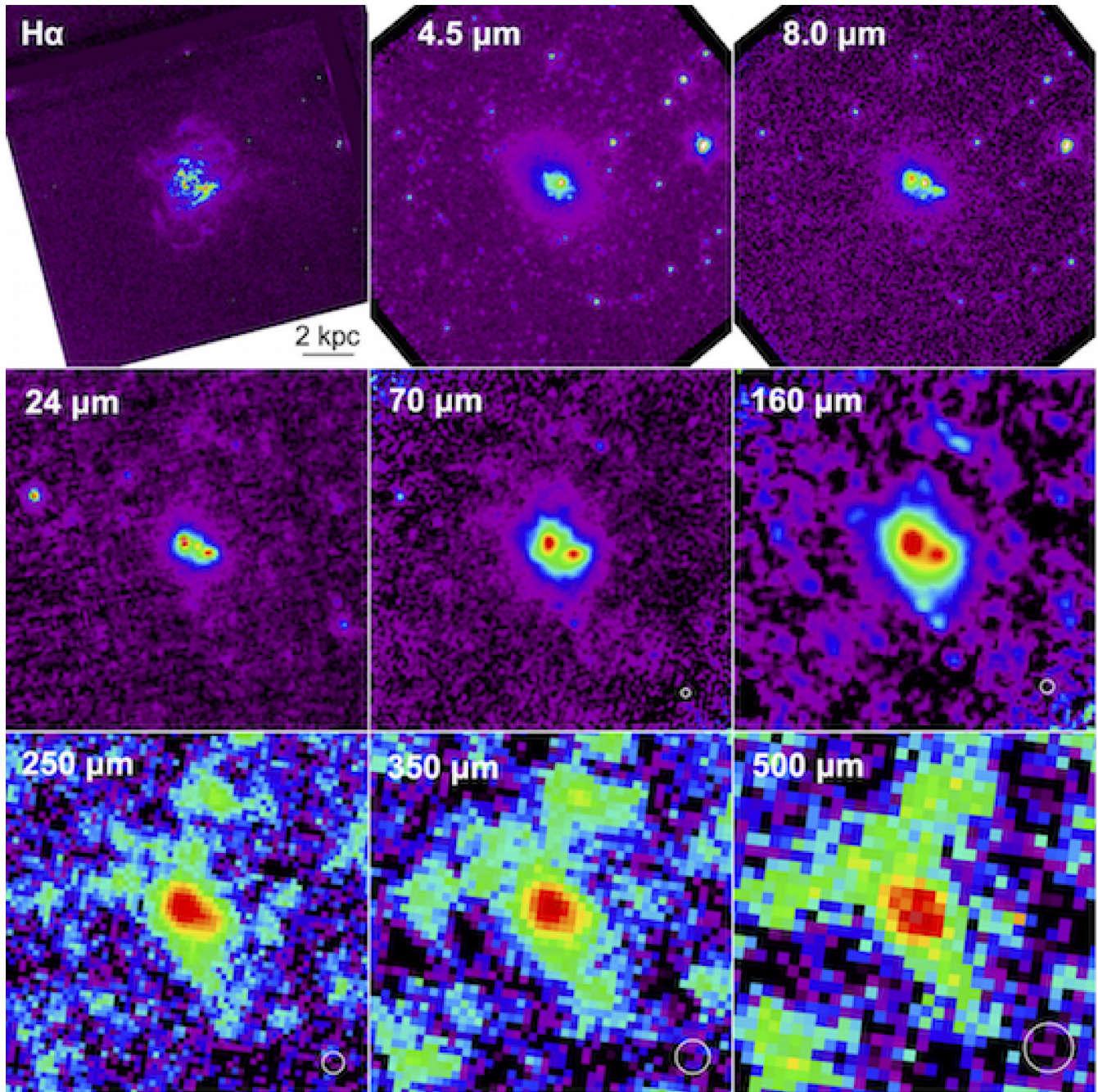
Figure 1 – *continued*

disc region into the circumgalactic region is added back into the disc flux total.

We also took sample flux measurements in darker, mostly source-free sky regions outside the global flux regions to confirm whether SCANAMORPHOS had properly removed the background in the *Herschel* maps. The background regions in the PACS maps contained flux values close enough to zero as to be indistinguishable from noise. However, the backgrounds of the SPIRE maps still contained enough flux from either background sources or residual noise to require a background correction. We measured the flux in background regions identical in size and shape to the global region tiled around the global region perimeter. The bottom row of panels in each of Figs 2(a)–(f) shows the SPIRE background regions. We then averaged these background fluxes and subtracted the average to get the final SPIRE global flux measurement. The SPIRE background contribution fell somewhere in the 2–14 per cent range (mean ∼8 per cent) with NGC 1569 as an outlier at about 35 per cent (weighted average of the regions shown in Fig. 2b), likely due to some contribution from nearby Galactic cirrus emission.

We adopted a conservative flux calibration uncertainty of 10 per cent, which consists of the systematic (4–5 per cent), statistical (1–2 per cent), and PSF/beam size (4 per cent) uncertainties. The aperture sizes of the global regions in our sample had radii

Figure 1 – *continued*

~110 arcsec. Derived aperture corrections of order ~3–4 per cent (Paper I, Balog et al. 2014) are small compared to this calibration uncertainty. Colour corrections[2] are on the order of 2–3 per cent (for sources with a temperature of ~30 K), which are also small compared with our 10 per cent flux uncertainty. For sources with temperatures closer to 20 K, the colour correction to the 70 μm PACS flux is 8 per cent. The global, disc, and circumgalactic flux values are listed in Table 4.
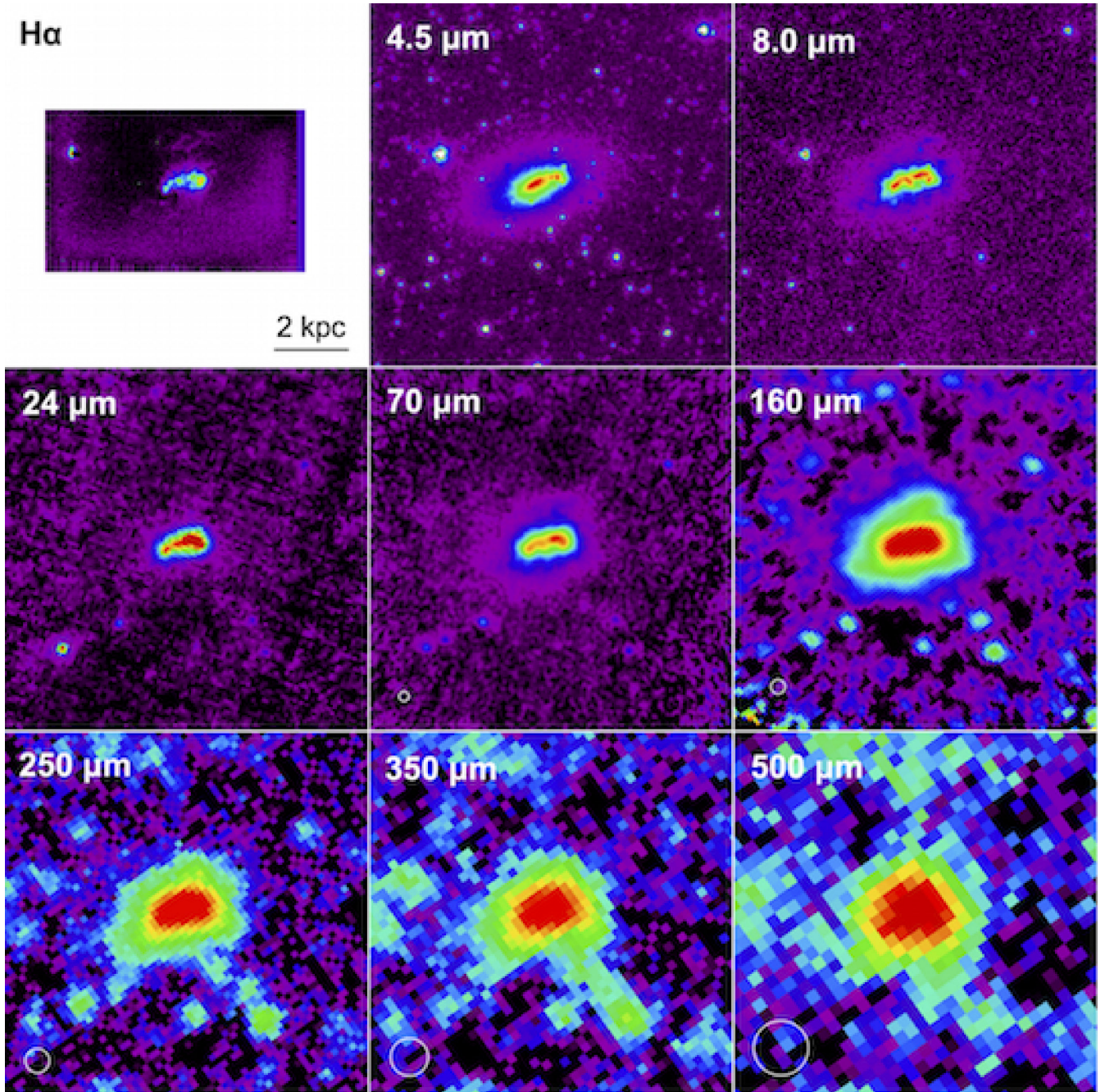
4.4 Spectral energy distribution fitting

In order to characterize the cold dust of each galaxy in our sample, we fit a modified blackbody (MBB) following the one found in section 3.1 of Smith et al. (2012). We fit the sets of 70, 160, 250, 350, and 500 μm global and disc flux values to:

$$S_\nu = \frac{M_d \, \kappa_\nu \, B_\nu(T_d)}{d^2}, \tag{1}$$

where M_d and T_d are the dust mass and temperature, respectively, d is the distance to the galaxy listed in Table 1, B_ν is the *Planck* function, and κ_ν is the dust absorption coefficient which has a power-law dependence with dust emissivity index β where $\kappa_\nu = \kappa_0(\nu/\nu_0)^\beta$.

---

[2] http://herschel.esac.esa.int/twiki/pub/Public/PacsCalibrationWeb/cc_report_v1.pdf

Figure 1 – *continued*

The constant κ_0 is the dust opacity at $\nu_0 = 350\,\mu$m: $0.192\,\text{m}^2\,\text{kg}^{-1}$ (Draine 2003). We fit the parameters M_d, T_d, and β to each set of global and disc fluxes to derive M_{global}, T_{global}, M_{disc}, and T_{disc}. The fits also included the 10 per cent flux calibration uncertainties. Fitting all three parameters often produced unphysical β values, so instead we fit just M_d and T_d and adopted a fixed value of $\beta = 2.0$, which is indexed to the dust opacity κ_0. Since the 70 μm flux value likely includes a contribution from a warmer dust component (Casey 2012), we treated it as an upper limit in our MBB fits. For consistency, we did not include the 100 μm flux values in the MBB fits, since these observations have not been done to match the depth of our 70 and 160 μm data. We estimated the uncertainties in the fit parameters by running 500 Monte Carlo MBB fits for each

set of fluxes, which we let vary randomly within the associated uncertainties for each run. Figs 4 and 5 show the global and disc MBB fits, respectively, with the disc MBB fits shown for fluxes both before and after application of the CLEAN algorithm. The MBB fit parameters and the uncertainties estimated with the Monte Carlo method are listed in Table 5.

We also tried fitting the circumgalactic flux values to the same single MBB, but these fits produced unphysical results (e.g. unrealistically high dust masses). We believe that this is due to the faint flux of the circumgalactic emission and the heterogeneous nature of this emission (e.g. filaments of different temperatures and masses which are not well represented by a single MBB). Perhaps a detailed superposition of MBBs could reproduce the combined circumgalactic
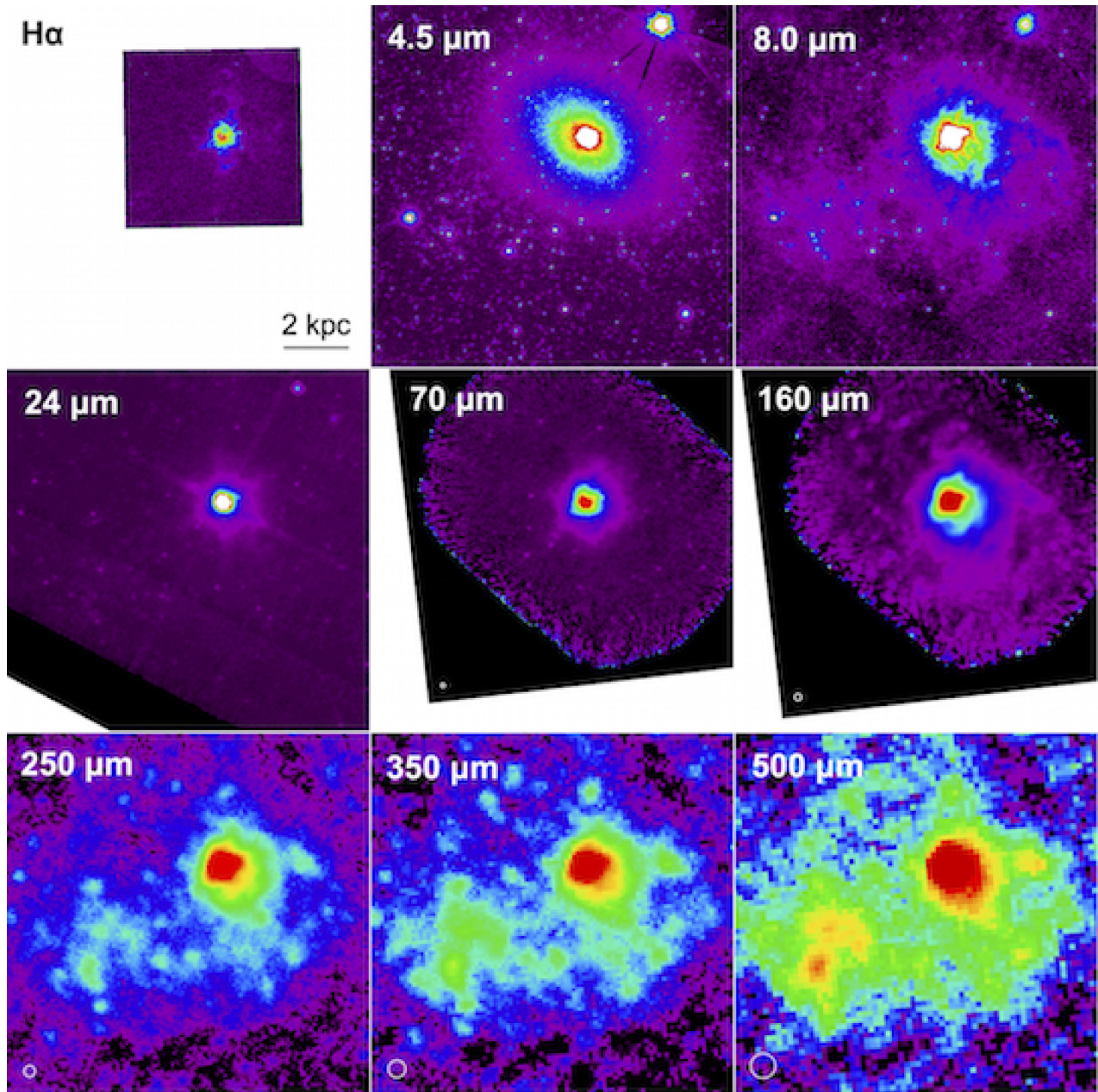
Figure 1 – *continued*

SED, but that avenue of analysis wades into more degenerate, subjective territory. To avoid this, we calculated the circumgalactic cold dust masses by simply using $M_{cg} = M_{global} - M_{disc}$.

The properties of the cold dust in the disc and circumgalactic regions depend on the value of the 4.5 μm surface brightness we adopted as the boundary between the disc and circumgalactic regions. For instance, choosing a higher 4.5 μ surface brightness of 0.3 MJy sr^{-1} instead of the favoured value of 0.1 MJy sr^{-1} for the disc–circumgalactic boundary produces a decrease of ∼10 per cent in the disc masses as well as an increase of ∼1 K in the disc temperatures when fitting the MBBs. However, since the disc masses (M_{disc}) are similar in magnitude to the global masses (M_{global}) and we used $M_{cg} = M_{global} - M_{disc}$, a small decrease in the disc mass produces a proportionally larger increase in the circumgalactic mass (M_{cg}). With

a surface brightness threshold of 0.3 MJy sr^{-1}, we found circumgalactic masses ∼50–100 per cent more massive than with the more conservative regions we have chosen. Therefore our choice of the larger, more conservative disc region does not significantly affect the derived disc properties, but does produce a more conservative circumgalactic dust mass.

5 RESULTS AND DISCUSSION

5.1 Morphology

We find circumgalactic dust features in all six galaxies of our sample (see Figs 2a–f and Appendix A). The most extended features range from 1.2 kpc (NGC 1800) to 2.6 kpc (He 2–10), as measured from the centre of the galaxy or from the mid-plane of the disc-like
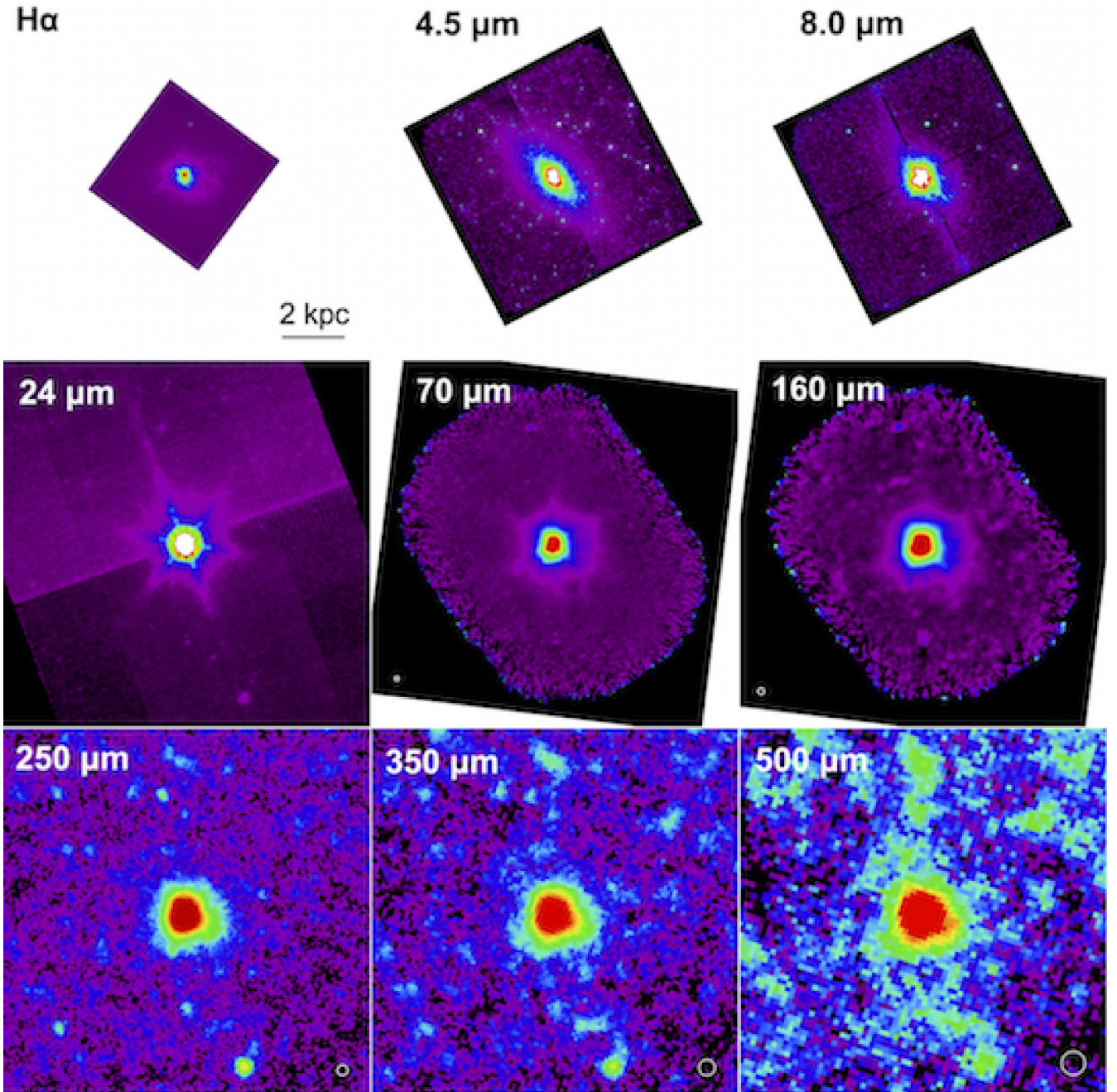
Figure 1 – *continued*

region out to the furthest part of the feature at the 3σ level above the background. These features extend to scales of $\sim$1.2–2.5 times the radii of the stellar component as measured by the 4.5 μm stellar disc region, and typically do not trace the orientation of the stellar disc. The circumgalactic features vary in morphology including extended filaments (NGC 1569, NGC 1705, NGC 1800, NGC 3077, and NGC 5253), clouds or knots of dust apparently separated from the disc region (NGC 1569, NGC 1705, and NGC 5253), as well as broader regions extending over a large range of galactocentric angles (e.g. He 2-10). As a member of the M81 group, NGC 3077 is in the process of interacting with M81 and M82, so much of

the circumgalactic cold dust features might be attributed to tidal stripping. In particular, the features to the east, west, and north–northeast of NGC 3077 are likely due to tidal stripping since 21-cm observations (Cottrell 1976; van der Hulst 1979; Yun, Ho & Lo 1994) show H I tidal streams in those regions.

Some circumgalactic cold dust features coincide with similar emission features in the ancillary Hα, 8.0, and 24 μm data (e.g. filaments of NGC 1569 and NGC 1800), but others do not (e.g. the broader plume extending south-southwest (SSW) from NGC 1705). Fig. 6 shows the 160 μm PACS maps overlaid with Hα contours based on the data listed in Table 3. The morphology of
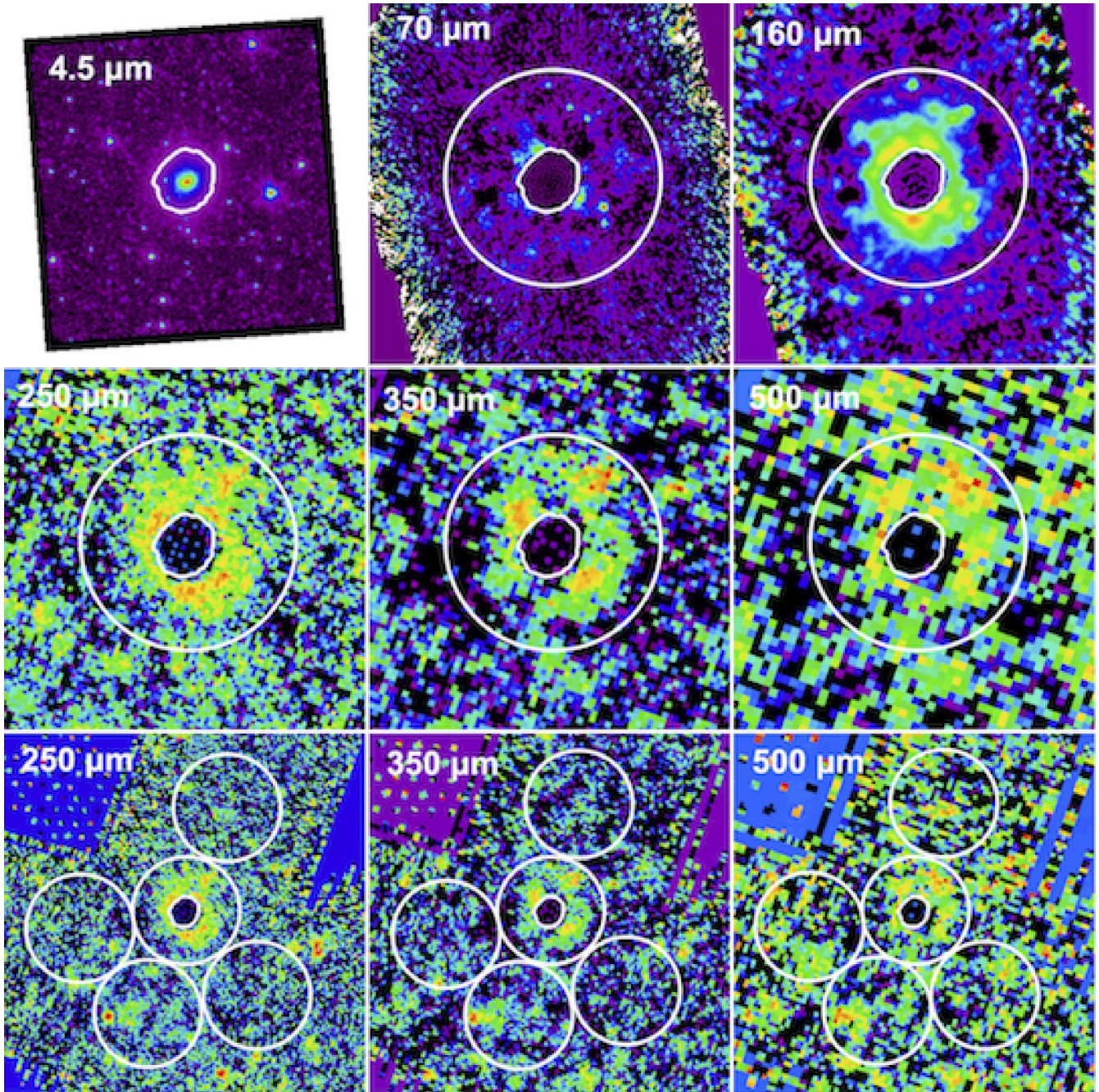
Figure 2. (a) *Herschel* maps of He 2–10 at 70, 160, 250, 350, and 500 μm after application of our CLEAN algorithm. The IRAC 4.5 μm map shows the stellar component for comparison. All images are displayed on a logarithmic intensity scale. North is up and east is to the left in all images. The inner white contour in the *Herschel* maps indicates the stellar disc region derived from the 4.5 μm data, while the white circle or ellipse shows the full extent over which the global infrared fluxes were calculated. The bottom row shows the SPIRE maps (250, 350, and 500 μm) and the circular or elliptical regions used to estimate the background flux in each band. The field of view of the panels in the bottom row is twice that of the six panels in the top and middle rows. (b) NGC 1569 – display is the same as in (a). (c) NGC 1705 – display is the same as in (a). (d) NGC 1800 – display is the same as in (a), plus one region is masked (smaller white circle). (e) NGC 3077 – display is the same as in (a). (f) NGC 5253 – display is the same as in (a).

the circumgalactic cold dust features does not always match the morphology of their warmer counterparts at shorter wavelengths. For example, the cold dust around NGC 1705 exhibits a somewhat filamentary morphology with a broad plume extending SSW and spatially extended emission to the north, while the Hα features are more shell-like as shown by the arcs of emission directly south and

north-west of the disc. The hot and warm wind components traced by Hα and PAH emission do not correlate exactly with the cold dust component, and therefore should not be used as a predictor of cold dust and vice versa. This result supports the idea of shielded regions within a galactic wind where dust may remain protected from sputtering via thermal, radiation, or collisional processes (e.g.
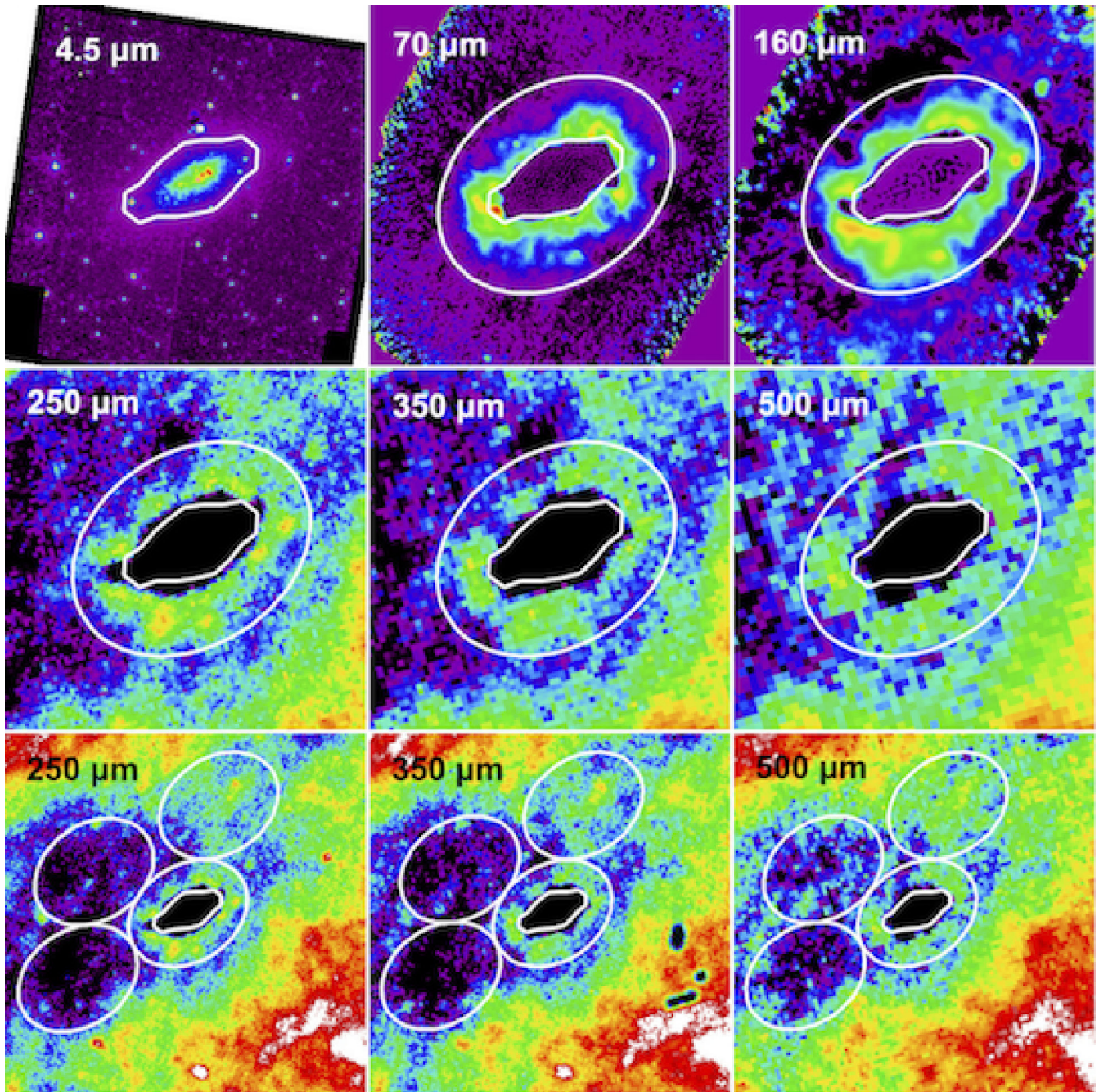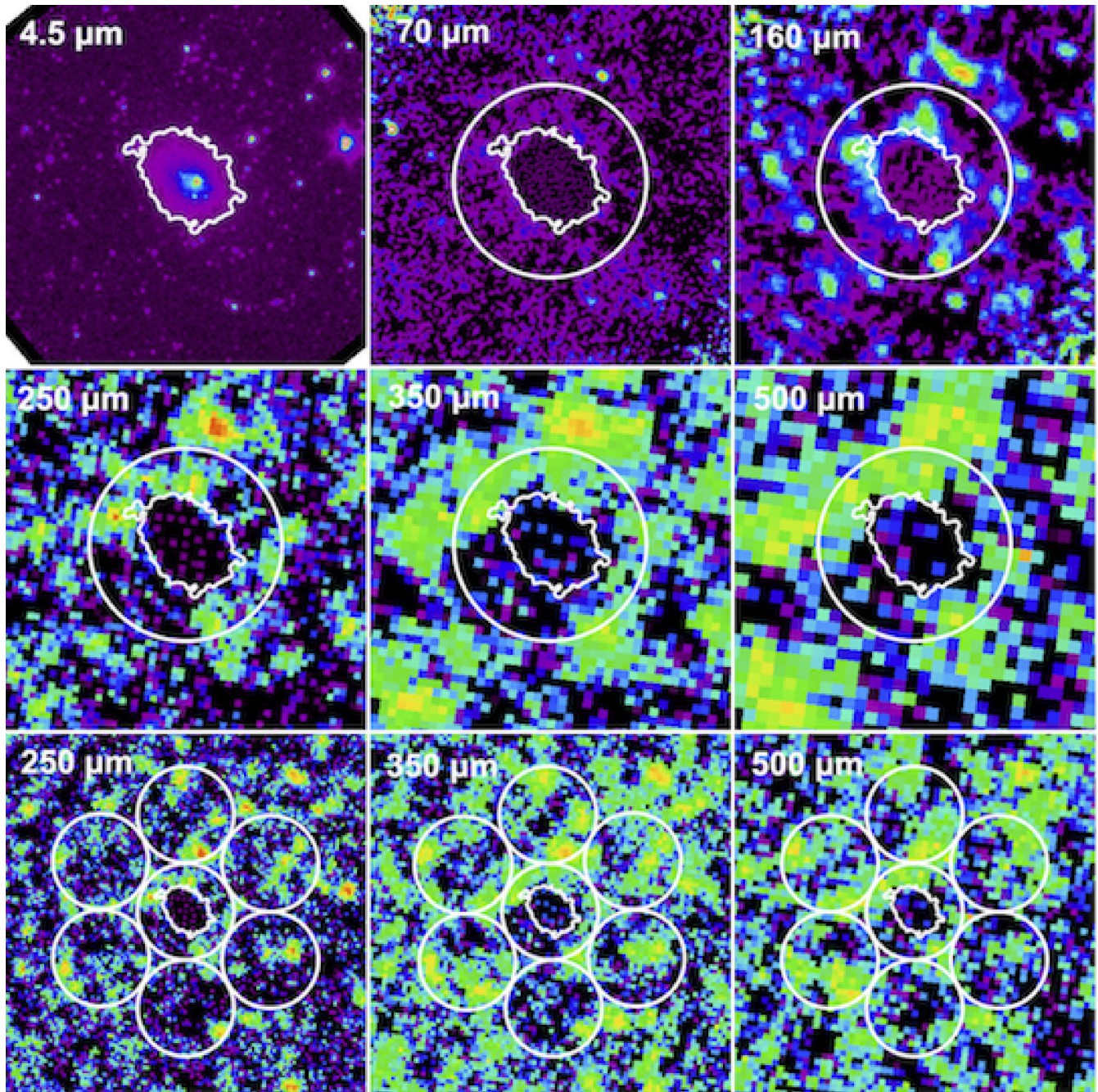
Figure 2 – *continued*

Jurac, Johnson & Donn 1998; Gnedin & Draine 2014). Appendix A contains further discussion of individual galaxies, their cold dust features, and comparisons with H I and X-ray observations.

5.2 70/160 μm ratio maps

In order to estimate the dust temperature and its spatial distribution using a proxy measurement, we made ratio maps where the 70 μm flux maps were divided by the 160 μm flux maps.[3] We first

---

[3] The dust emissivity, β, and dust grain size distribution can also contribute to variations in 70/160 μm ratios (see Paper I).

convolved the 70 μm maps to the pixel scale of the 160 μm maps using the convolution kernels described in Aniano et al. (2011). We then aligned the resulting convolved images with the 160 μm maps and took the ratio, limiting the plotted ratios to pixels where the 160 μm map had values >0.0001 Jy pixel^{-1} ($\sim 1\sigma$ above the background) for the sake of clearly displaying galactic features. The 70/160 μm ratio maps are shown in Fig. 7. All of the galaxies exhibit warmer dust temperatures (ratio >1.0) near their nuclei as would be expected for the stronger radiation field in nuclear regions, while their outer regions tend to appear cooler. Unlike the other galaxies, NGC 3077 has a striking temperature gradient along the northeast to southwest axis. Observations have shown that the tidal features of NGC 3077 are significantly cooler than the galaxy itself (Walter
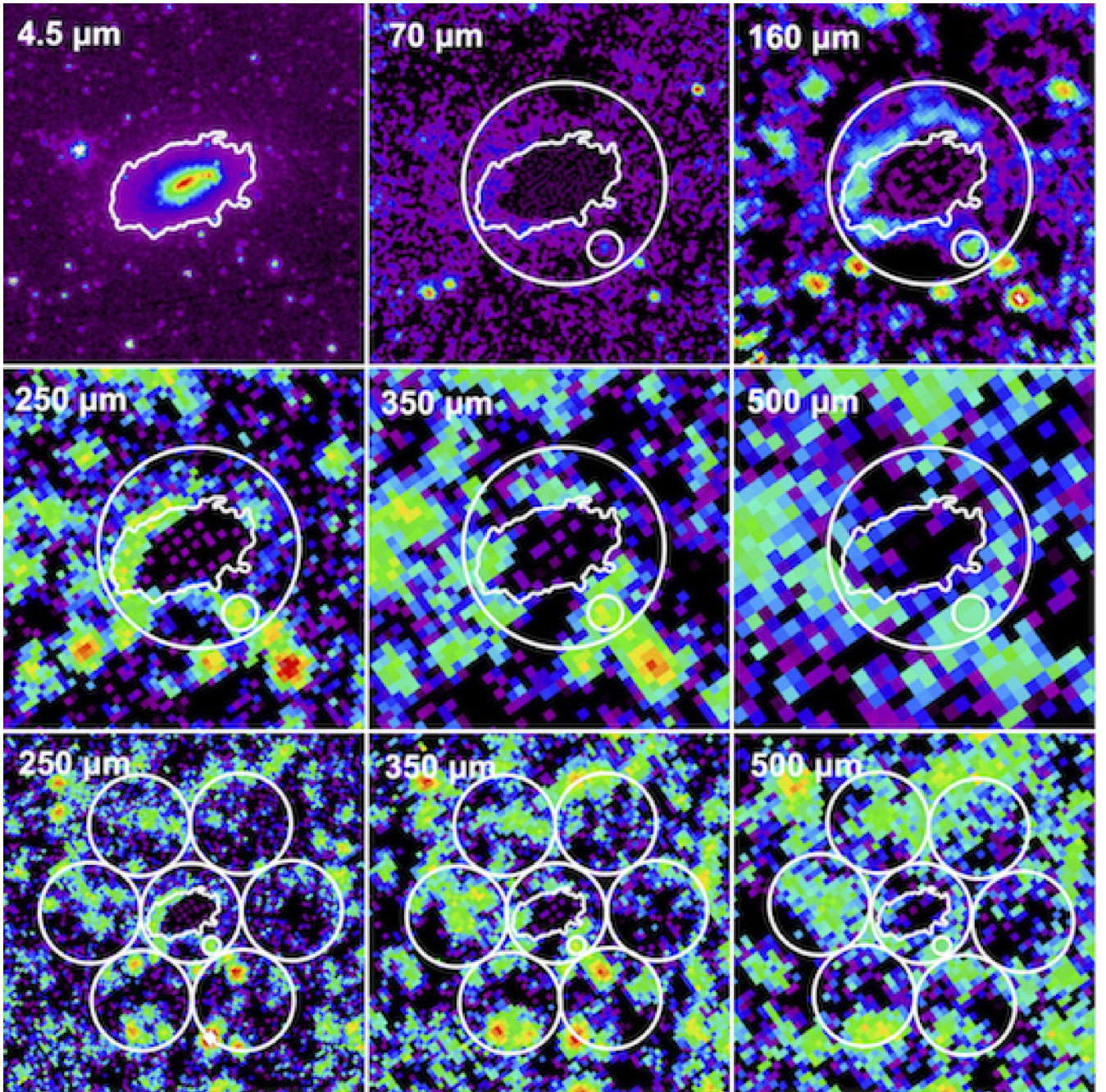
Figure 2 – *continued*

et al. 2011). The cooler dust to the southwest of the nucleus appears to coincide with warm dust in the 8.0 and 24 μm maps and the H I tidal stream towards M81 (Cottrell 1976; van der Hulst 1979; Yun et al. 1994), but no obvious Hα feature. In general, the warmer regions in the ratio maps shown by yellow and red colours in Fig. 7 do not appear to correlate well in a qualitative sense with much of the warm dust features in the 8.0 and 24 μm maps or hot ionized gas of the Hα maps, though some exceptions arise like the bright filament to the southwest of NGC 1569 and the warmer region to the east of the nucleus in NGC 5253 coinciding with the ionization cone reported by Zastrow et al. (2011). Finally, the temperature structure of He 2–10 is highly peaked at the centre, perhaps due to AGN activity in its nucleus (Reines et al. 2011, 2016).

5.3 Global gas-to-dust ratios

Table 5 lists the cold dust masses and temperatures derived by fitting MBB to the FIR emission from the global and disc regions (Section 4.4). The fitted global cold dust masses are in the range $\sim 10^5$–$10^{6.5}$ M$_\odot$. For comparison, the total gas masses (H I + H$_2$) for the galaxies in our sample lie in the range ~ 1.5–9.0×10^8 M$_\odot$ (Table 1), implying gas-to-dust ratios of ~ 200–1500. These elevated values compared with that of the Milky Way (gas-to-dust ratio of ~ 140; e.g. Draine et al. 2007) confirm recent results by Rémy-Ruyer et al. (2014); Rémy-Ruyer et al. (2015) and Feldmann (2015) that low-metallicity dwarf galaxies are deficient in dust compared to our own Galaxy.

Figure 2 – *continued*

5.4 Comparison with the host galaxy properties

As discussed in Section 4.4, we calculated the circumgalactic cold dust mass (M_{cg}) listed in Table 5 by subtracting the disc cold dust mass (M_{disc}) from the global cold dust mass (M_{global}). Fig. 8 shows M_{cg} versus the total baryonic (stellar plus gas) mass for the galaxies in our sample. The stellar masses (M_*) are listed in Table 1 and were calculated using the same method as Zastrow et al. (2013, , see Table 1 for more detail). The circumgalactic dust exhibits a weak (Pearson's $r = 0.80$; P[null] $= 0.055$) positive linear correlation with the baryonic mass. This correlation should be considered with caution, since it is based on a sample of only six objects (this issue is discussed in more detail below). If real, this positive correlation

may reflect one of two things: (1) that bigger, more massive galaxies simply have more of everything, including stars, gas, and dust, inside and outside of their stellar discs, or (2) there is actually a physical connection between the deposition of the dust in the circumgalactic environment via star formation-driven winds or tidal processes and the processes associated with the stellar build-up of galaxies.

In an attempt to differentiate between these two scenarios, we plot M_{cg} normalized by M_{global} versus the SFR surface density (Σ_{SFR}, see Table 1) in Fig. 9. This last quantity is estimated using the (infrared + Hα) SFR (based on the prescription of Kennicutt et al. 2009) together with the extent of the Hα emission ($R_{H\alpha}$) listed in
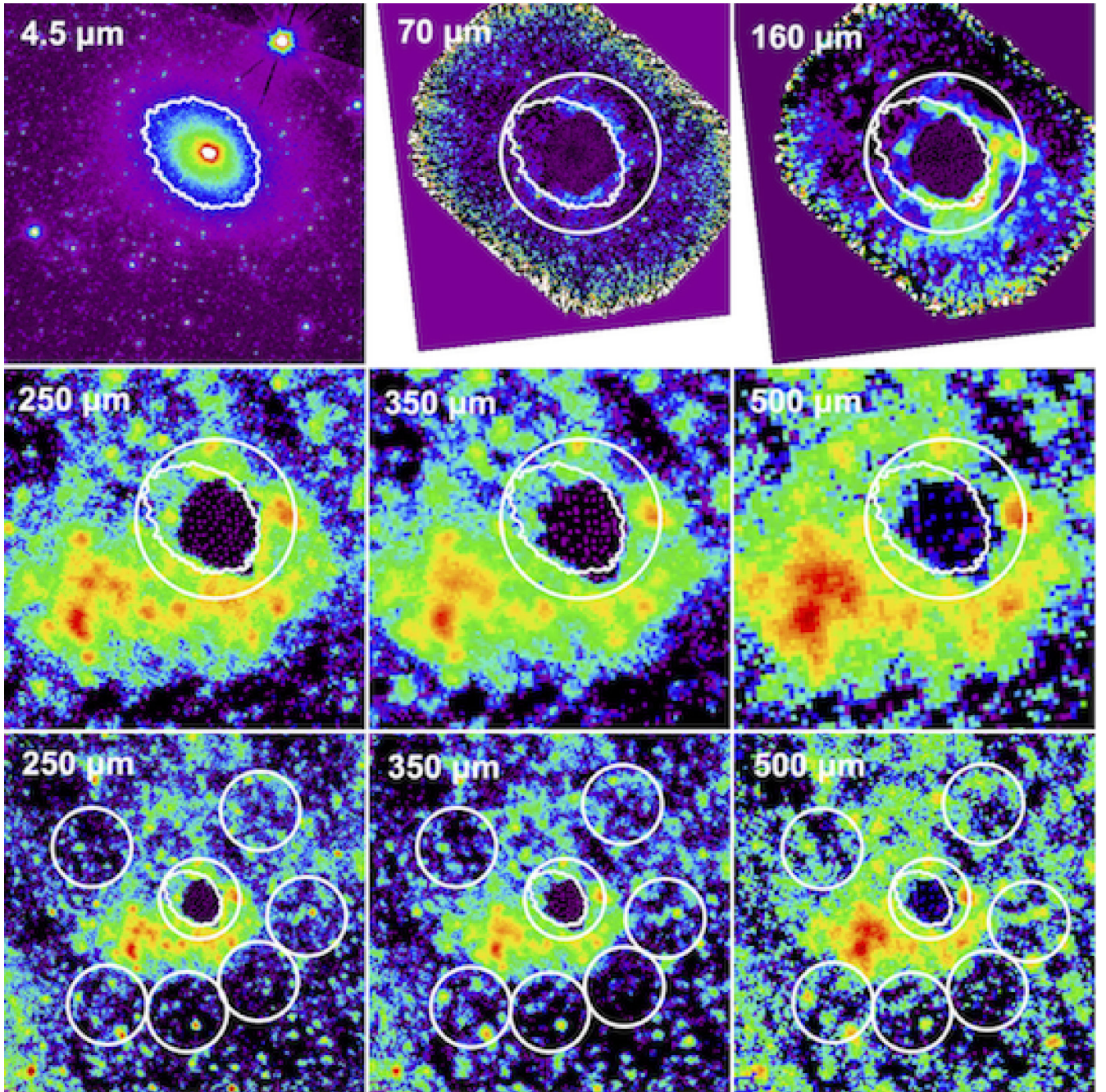
Figure 2 – *continued*

table 1 of Calzetti et al. (2010).[4] Keeping in mind that the typical
dust mass uncertainties from the MBB fitting are on the order of
~40 per cent, Fig. 9 shows that typically ~10–20 per cent of the cold
dust in these wind-hosting dwarf galaxies lies in the circumgalactic
region. NGC 1569 is an outlier, having as much as ~60 per cent of
its cold dust in the circumgalactic region. Overall, Fig. 9 shows no
obvious trend, contrary to what might be naively expected if the
dust is lifted above the disc by energy inputs from star formation

activity in the disc. We caution against drawing general conclu-
sions about dwarf galaxies based on a sample of only six objects.
Furthermore, we note that the lack of a trend in Fig. 9 is not un-
expected if the stellar mass–metallicity relation in low-mass dwarf
galaxies is due to inefficient conversion of gas into stars in these ob-
jects rather than supernova-driven outflows (e.g. Tassis, Kravtsov &
Gnedin 2008).

Other factors may also be affecting our results. One possibility is
that our measurements might be missing the very cold dust in giant
molecular clouds within the disc, thus overestimating the fraction
of dust found in the circumgalactic region. However, this cannot ex-
plain the large circumgalactic dust mass fraction measured in NGC
1569 since the H_2 gas mass is only about 1 per cent of the H I gas

---

[4] Note again that an AGN may contribute to the FIR emission in He 2–10,
so its SFR and global and circumgalactic dust masses carry that caveat,
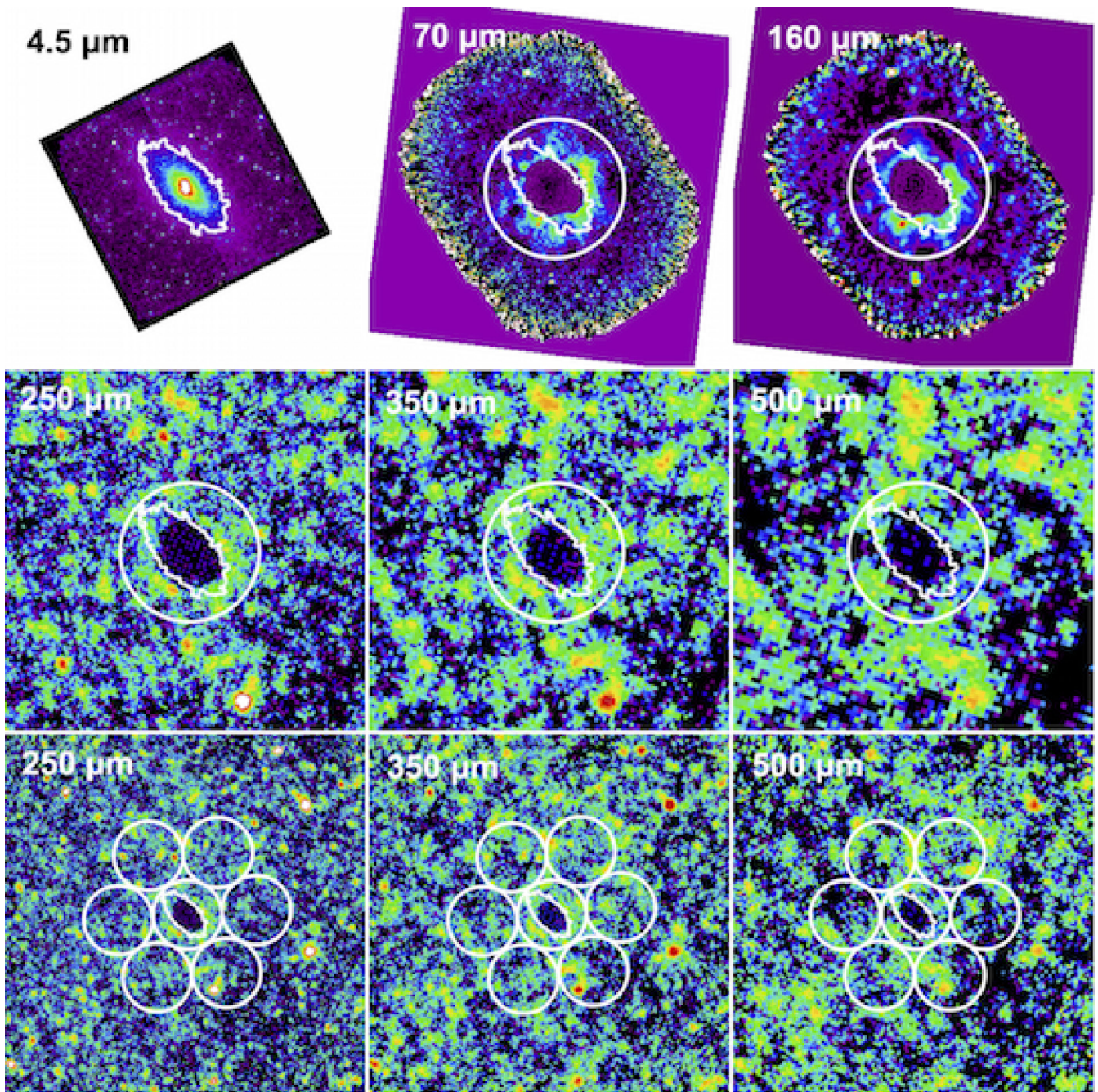indicated by the open red circle in Figs 8–10.

Figure 2 – *continued*

mass in this object (see Table 1), and thus there are very few hiding places for additional dust in the disc. A more valid concern about NGC 1569 is contamination from Galactic cirrus emission. While the sky immediately surrounding NGC 1569 appears mostly free of Galactic cirrus in the SPIRE bands, there is indeed significant cirrus emission in adjacent regions. Our estimate of the background and foreground flux attempts to account for this potential contamination by including a region (upper right ellipse in Fig. 2b) which includes some cirrus emission. If foreground emission from Galactic cirrus happened to be projected against the circumgalactic region of NGC 1569 and not the disc region, then M_{cg}/M_{global} would be overestimated. However, we find that this convoluted scenario is unlikely to fully explain the large value of M_{cg}/M_{global} given the clear detection

in Fig. 3 of the circumgalactic dust emission not only at 250, 350, and 500 μm but also at 70 and 160 μm, where cirrus emission is no longer an issue.

Another potential source of scatter in Fig. 9 is the presence of dusty tidal streams contributing to the circumgalactic FIR emission. NGC 3077 is the clearest case of a tidally disrupted dwarf in our sample, where this effect is likely important. Karachentsev & Makarov (1999) developed a tidal index parameter (Θ_i) as a quantitative measure of the importance of tidal effects based on the masses and three-dimensional distances from its nearest neighbours. The maximum value of Θ_i determines the galaxy's 'Main Disturber' (MD). A maximum Θ_i greater than zero indicates gravitational interaction with the MD within a tidal radius, while a value less than
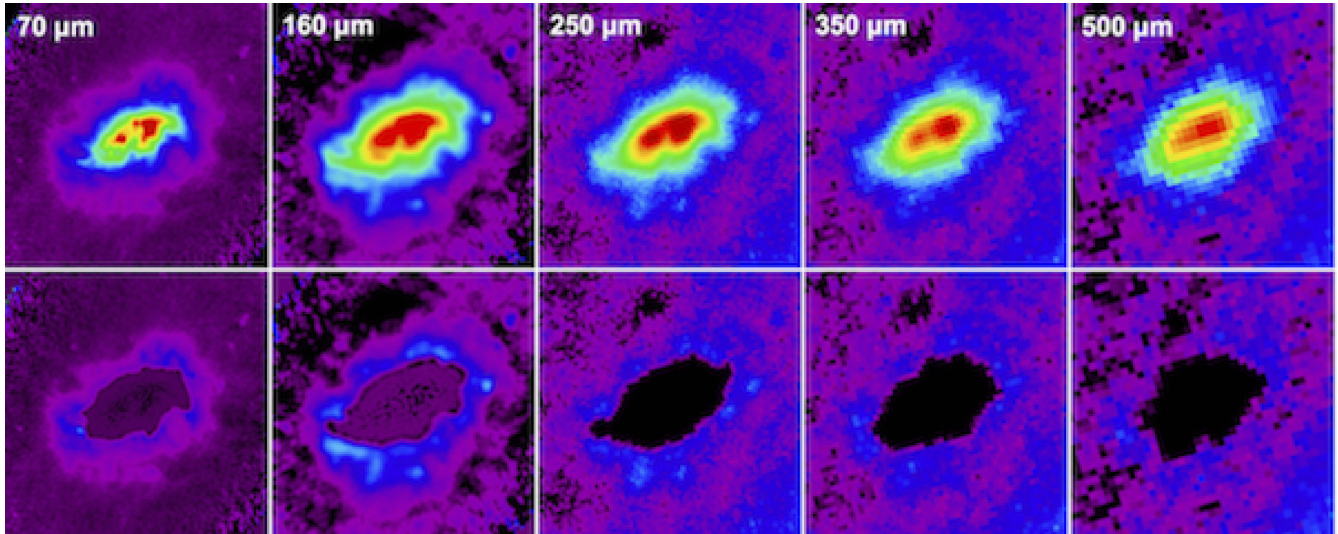
Figure 3. Top row shows the PACS and SPIRE maps of NGC 1569 while the bottom row shows the resulting residual maps after application of our modified CLEAN algorithm. We defined the regions where we applied the CLEAN algorithm in each band based on the stellar disc region for NGC 1569. Since each map has a different pixel scale and slightly different morphology to the bright disc areas, the regions where we applied the CLEAN algorithm are similar in extent but necessarily slightly different from band to band. All maps are shown on logarithmic intensity scale. North is up and east is to the left in all maps.

Table 4. Global, disc, and circumgalactic infrared fluxes[a].

Galaxy	Global[b] (Jy)					Disc[c] (Jy)					Circumgalactic[d] (Jy)				
	70	160	250	350	500	70	160	250	350	500	70	160	250	350	500
He 2–10	24.206	19.260	6.696	2.543	0.878	24.067	18.225	6.097	2.198	0.801	0.139	1.035	0.599	0.345	0.077
NGC 1569	55.466	37.953	13.462	5.659	2.040	52.945	35.007	8.399	3.043	1.183	2.521	2.946	5.063	2.616	0.857
NGC 1705	1.234	1.372	0.593	0.292	0.125	1.082	1.142	0.458	0.227	0.107	0.152	0.230	0.135	0.065	0.018
NGC 1800	1.048	1.900	0.909	0.436	0.182	0.968	1.660	0.768	0.384	0.176	0.080	0.240	0.141	0.052	0.006
NGC 3077	17.897	22.071	10.115	4.204	1.539	17.888	21.299	8.967	3.581	1.324	0.009	0.772	1.148	0.623	0.215
NGC 5253	30.740	21.540	8.212	3.709	1.466	30.067	20.519	7.478	3.369	1.341	0.673	1.021	0.734	0.340	0.125

[a]The tabulated fluxes have a calibration uncertainty of ± 10 per cent.

[b]The global fluxes measured in the 250, 350, and 500 μm SPIRE maps include background corrections (see Section 4.3).

[c]The cleaned disc fluxes are calculated as: global fluxes − cleaned circumgalactic fluxes (see Section 4.3).

[d]The circumgalactic fluxes are measured from the CLEAN residual maps (see Section 4.3).

zero indicates a relatively isolated galaxy outside that tidal radius. Amongst our sample, NGC 1569, NGC 3077, and NGC 5253 have positive Θ_i values (Karachentsev, Kaisina & Makarov 2014), of which NGC 3077 unsurprisingly has the highest value. In contrast, He 2–10, NGC 1705, and NGC 1800 all have negative Θ_i, indicating their isolation and thus likely negligible contributions from tidal streams to the measured circumgalactic dust. Our data do not show any systematic difference in M_{cg}/M_{global} between these two groups of objects.

If the dust in a galaxy carries fractionally more metals than its gas, then dust infall on to a galaxy or outflow from the galaxy can significantly affect the overall ISM metallicity of the host (e.g. Spitoni et al. 2010).[5] We determined the gas metallicity $(12 + \log(O/H))$ for each galaxy in our sample using the emission-line method developed in Pettini & Pagel (2004) (using ([O III]/Hβ)/(N II/Hα)) with emission-line strengths from a few sources (see Table 1). In order to compare these gas metallicities with the mass–metallicity relation derived in Tremonti et al. (2004),

we used the metallicity calibration conversion found in Kewley & Ellison (2008) to calculate analogous values, taking into account the ~0.1 dex uncertainty in the Pettini & Pagel (2004) method as well as the ~0.06 dex uncertainty in the conversion (Kewley & Ellison 2008). The converted values are listed in Table 1. The mass–metallicity relation derived in Tremonti et al. (2004) is $12 + \log(O/H)_{predicted} = -1.492 + 1.847(\log M_*) - 0.08026(\log M_*)^2$, where O/H is the oxygen abundance and M_* is the stellar mass in units of solar masses. The equation is valid over the mass range $8.5 < \log(M_*/M_\odot) < 11.5$. We used this relation and the M_* values listed in Table 1 to calculate the predicted value of $12 + \log(O/H)_{predicted}$. We have taken solar metallicity to be $12 + \log(O/H) = 8.69$ (Allende Prieto, Lambert & Asplund 2001).

In Fig. 10, we calculate a metallicity deficit $(\Delta \log(O/H))$ by subtracting $12 + \log(O/H)_{predicted}$ from the value derived from the emission-line strengths and compare that to M_{cg}/M_{global}. In NGC 3077 and He 2–10, dusty tidal streams and AGN should be considered respectively when interpreting Fig. 10. The tidal streams of NGC 3077 likely increase M_{cg}/M_{global}, even though our observations do not cover the entire spatial extent of the streams when compared with the H I data (Cottrell 1976; van der Hulst 1979; Yun et al. 1994; Walter et al. 2011). The AGN in He 2–10 (Reines et al. 2011, 2016) may eject and heat dust more efficiently, thus increasing M_{cg}/M_{global}.

[5] Note, however, that the detail of how the outflowing material interacts with the surroundings and perhaps regulates the inflow rate of gas is still subject to an active debate (Tassis et al. 2008; Feldmann 2015).
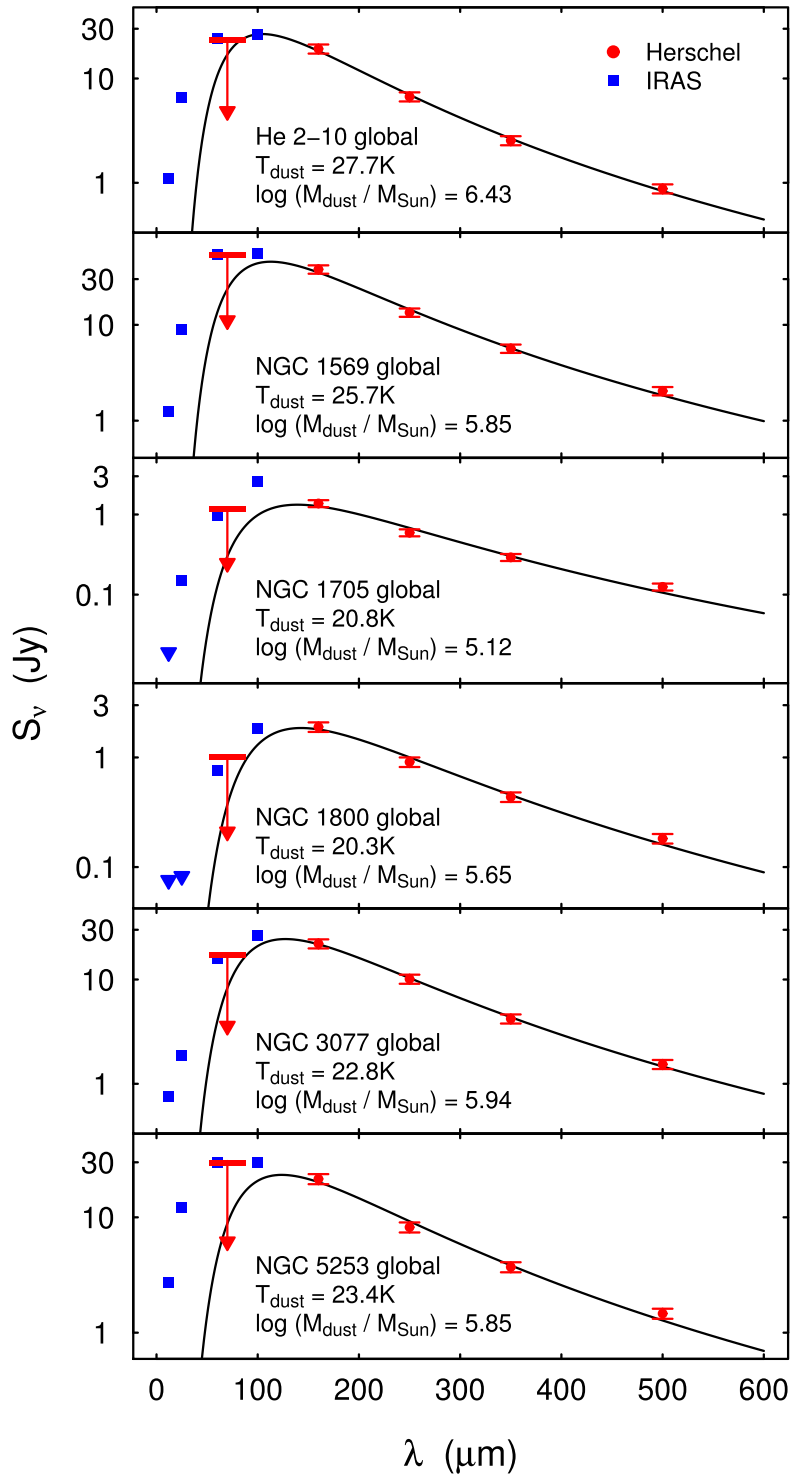
Figure 4. MBB fits (shown as black curves) to the global galaxy fluxes derived from the 70, 160, 250, 350, and 500 μm *Herschel* data (shown as red points). In this fitting, the 70 μm flux values were treated as upper limits as indicated by the downward arrows. The fit parameters are M_{dust} and T_{dust}. Refer to Section 4.4 for details. The blue squares mark the *IRAS* fluxes at 12, 25, 60, and 100 μm (Moshir et al. 1990; Sanders et al. 2003), while the blue downward triangles represent upper limits. The MBB fits do not include the *IRAS* flux values, since these data are shallower than our *Herschel* maps.

Also, the presence of the AGN may raise [O III]/Hβ resulting in an underestimate of the actual log(O/H) value for this object. Keeping these considerations for He 2–10 and NGC 3077 in mind, we find that the galaxy with the largest metallicity deficit, NGC 1569, also has the largest fraction of circumgalactic dust. In this context, it is interesting to note that the amount of metals locked in the cold dust outflow of NGC 1569 we found with our MBB fits (4.5×10^5 M$_\odot$, assuming most of the dust mass is in metals) is ∼10 times larger than the mass of oxygen detected in its hot outflow (3.4×10^4 M$_\odot$; Martin et al. 2002).
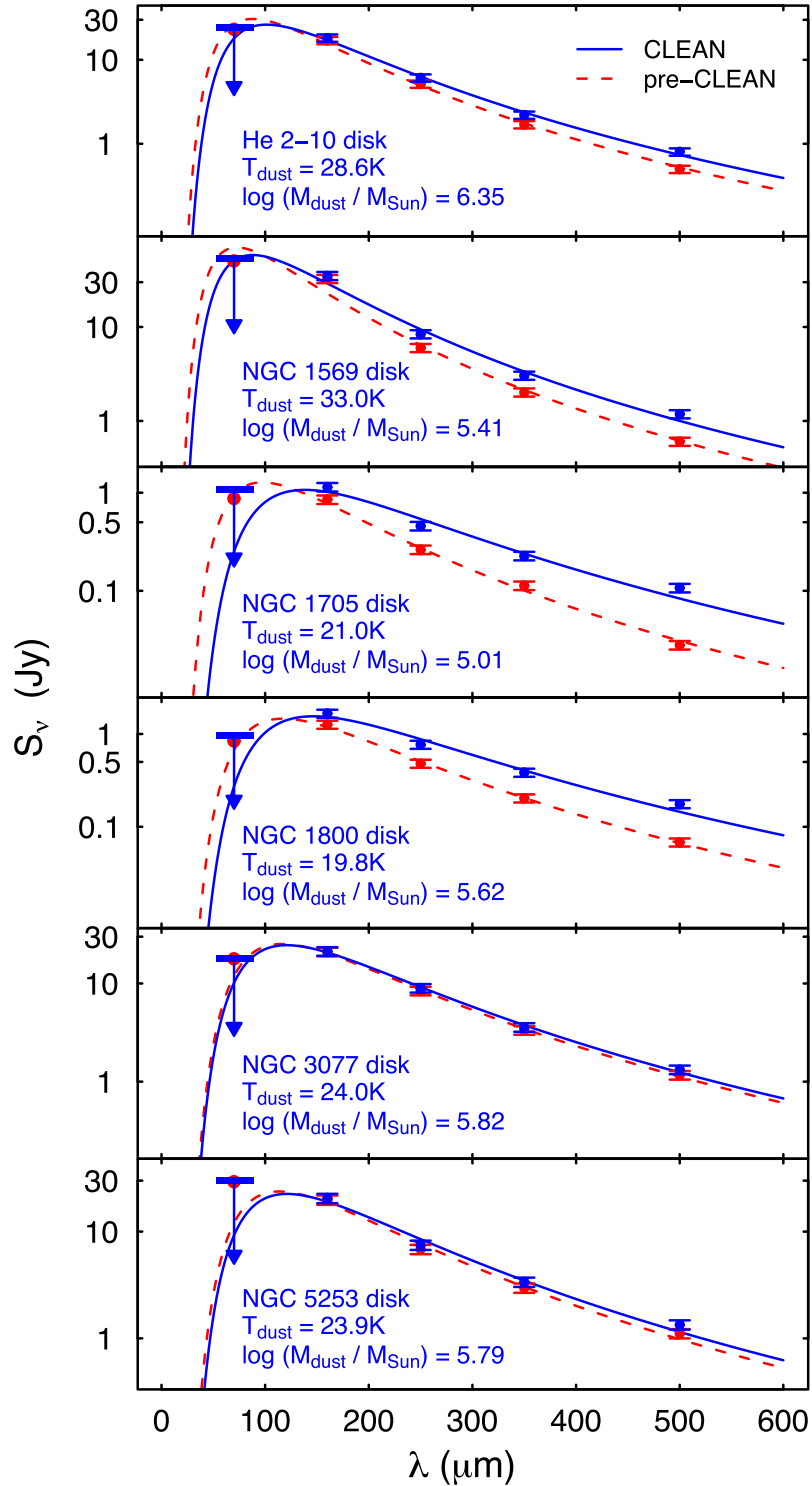
Figure 5. MBB fits to the galaxy disc fluxes derived from the 70, 160, 250, 350, and 500 μm *Herschel* maps before (dashed red line) and after (solid blue line) applying our modified CLEAN algorithm. In the fitting, the 70 μm flux values were treated as upper limits as indicated by the downward arrows. The fit parameters are M_{dust} and T_{dust}. Refer to Section 4.4 for details.

Overall, the small number of objects in our sample and the rather large uncertainties on $\Delta \log(O/H)$ and M_{cg}/M_{global} preclude us from drawing any statistically significant conclusions. Furthermore, recent results have warned of the increased scatter in the mass-metallicity relation at lower masses (e.g. Zahid et al. 2012;

Paalvast & Brinchmann 2017), which may further cloud the issue. Finally, as noted previously, the extent of the H I in dwarf galaxies is known to differ significantly from the stellar component. Therefore, using the stellar component to define an edge or border for the galaxy remains an imperfect method of determining what is

Table 5. Fits to the SEDs.

	Global			Disc			Circumgalactic[a]	Circumgalactic/global[b]
Galaxy	$\log\left(\dfrac{M_{\mathrm{global}}}{\mathrm{M}_\odot}\right)$	β^c	T_{dust}	$\log\left(\dfrac{M_{\mathrm{disc}}}{\mathrm{M}_\odot}\right)$	β^c	T_{dust}	$\log\left(\dfrac{M_{\mathrm{cg}}}{\mathrm{M}_\odot}\right)$	$\dfrac{M_{\mathrm{cg}}}{M_{\mathrm{global}}}$
He 2–10	$6.43\,^{+0.042}_{-0.047}$	2.00	27.7 ± 1.2	$6.35\,^{+0.062}_{-0.073}$	2.00	28.6 ± 1.8	$5.64\,^{+100\ \mathrm{per\ cent}}_{-100\ \mathrm{per\ cent}}$	0.161 ± 0.030
NGC 1569	$5.85\,^{+0.061}_{-0.071}$	2.00	25.7 ± 1.4	$5.41\,^{+0.116}_{-0.158}$	2.00	33.0 ± 4.5	$5.65 \pm 30\ \mathrm{per\ cent}$	0.633 ± 0.216
NGC 1705	$5.12\,^{+0.149}_{-0.228}$	2.00	20.8 ± 4.2	$5.01\,^{+0.242}_{-0.593}$	2.00	21.0 ± 6.7	$4.47\,^{+320\ \mathrm{per\ cent}}_{-100\ \mathrm{per\ cent}}$	0.222 ± 0.189
NGC 1800	$5.65\,^{+0.074}_{-0.090}$	2.00	20.3 ± 1.3	$5.62\,^{+0.227}_{-0.504}$	2.00	19.8 ± 6.9	$4.39\,^{+1200\ \mathrm{per\ cent}}_{-100\ \mathrm{per\ cent}}$	0.056 ± 0.040
NGC 3077	$5.94\,^{+0.045}_{-0.050}$	2.00	22.8 ± 1.2	$5.82\,^{+0.040}_{-0.044}$	2.00	24.0 ± 0.8	$5.29 \pm 58\ \mathrm{per\ cent}$	0.227 ± 0.033
NGC 5253	$5.85\,^{+0.104}_{-0.136}$	2.00	23.4 ± 2.2	$5.79\,^{+0.102}_{-0.134}$	2.00	23.9 ± 2.1	$4.98\,^{+270\ \mathrm{per\ cent}}_{-100\ \mathrm{per\ cent}}$	0.133 ± 0.050

[a]The circumgalactic dust mass was determined by subtracting the disc dust mass from the global dust mass (see Section 4.4). The uncertainties on the circumgalactic dust mass come from the uncertainties on the global and disc dust masses added in quadrature. [b]The uncertainties on the circumgalactic-to-global dust mass ratios come from the *fractional* uncertainties on the global and disc dust masses added in quadrature. [c]The β values were fixed at 2.00 (see Section 4.4).
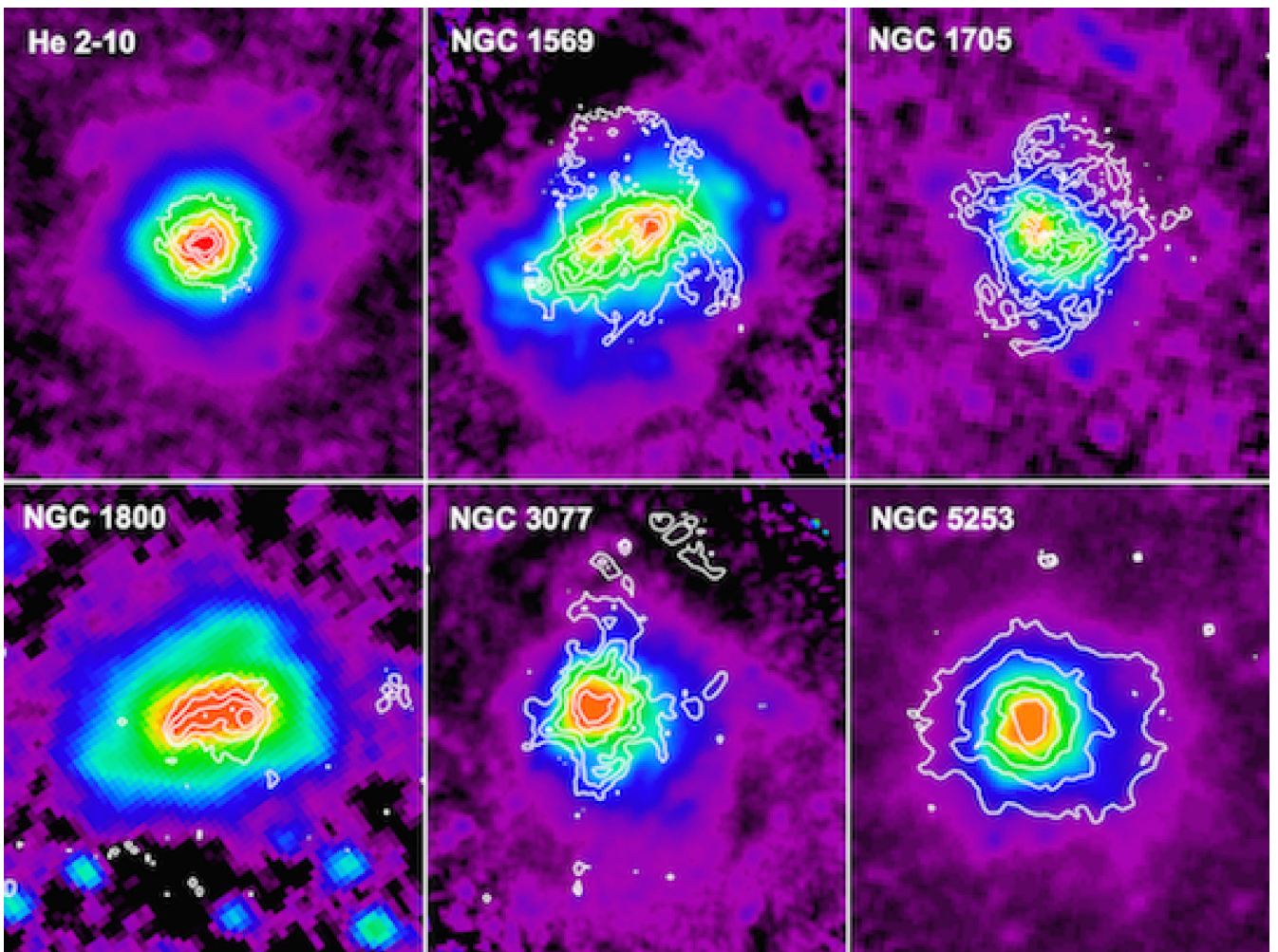
Figure 6. PACS 160 μm maps overlaid with Hα contours to compare the distribution of the cold dust with that of the warm ionized material. The field of view (FOV) of each panel is different to show the details at both 160 μm and Hα. FOV: He 2–10 3.96 arcmin × 4.46 arcmin; NGC 1569 4.79 arcmin × 5.40 arcmin; NGC 1705 3.13 arcmin × 3.53 arcmin; NGC 1800 2.64 arcmin × 2.98 arcmin; NGC 3077 5.23 arcmin × 5.89 arcmin; and NGC 5253 4.01 arcmin × 4.52 arcmin.

'inside' versus 'outside' of the galaxy. This is clearly an issue in NGC 3077 and also perhaps in NGC 1569 (e.g. Johnson et al. 2012; Johnson 2013). In addition, the lack of velocity information in our data makes it challenging to attribute circumgalactic dust features

to the known winds. Attempts to link the cold dust features detected in the *Herschel* maps with other dust tracers with kinematic information such as infrared H_2 and mm-wave CO transitions, Na I D 5890, 5896 Å, and H I 21 cm may provide a way around the lack of
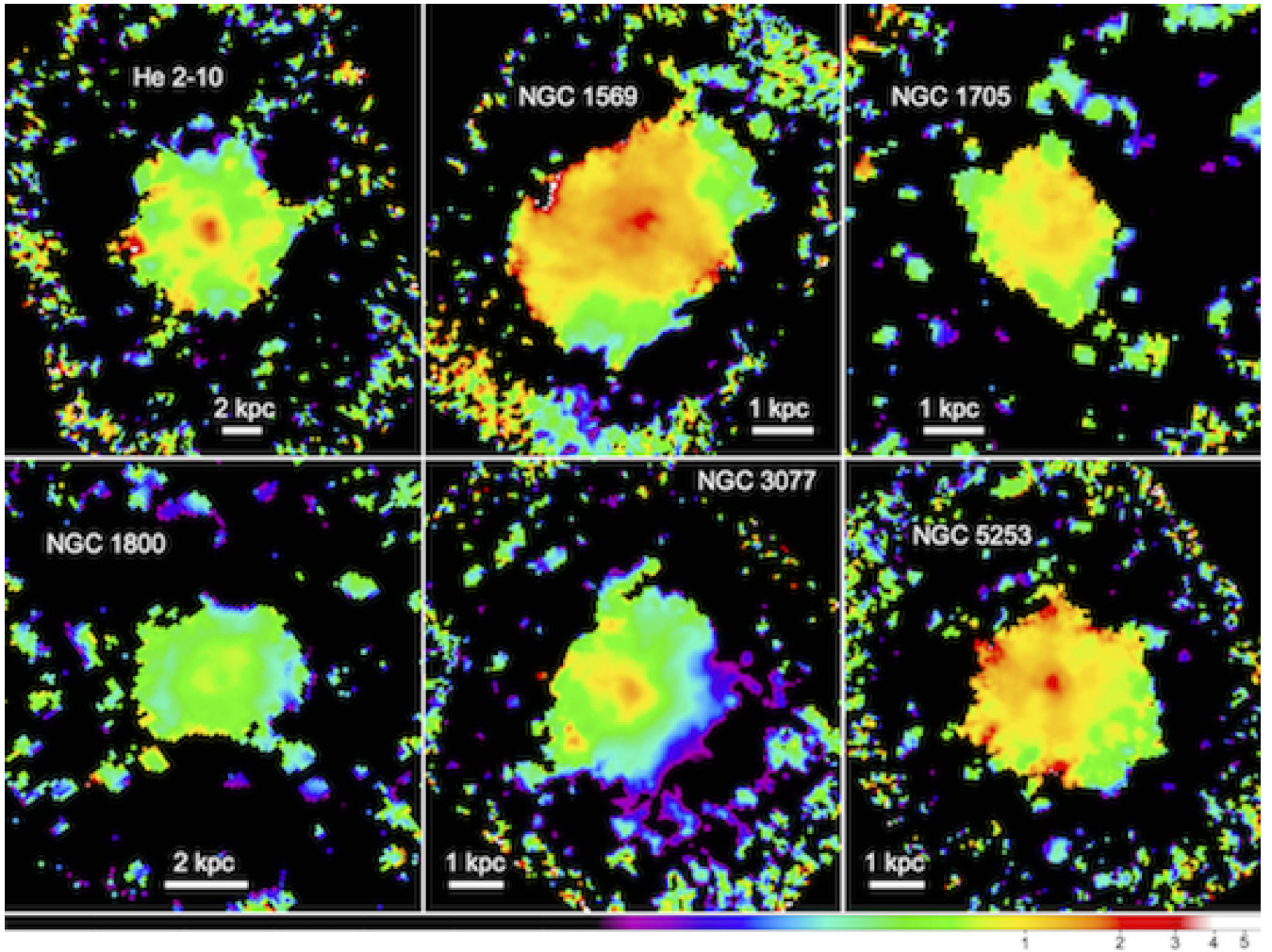
Figure 7. PACS 70/160 μm flux ratio maps. All maps are shown on the same logarithmic scale indicated by the colour bar. The white bar in each panel indicates the scale of each image. North is up and east is to the left in all images.

direct kinematic constraints on the cold dust component and a more concrete link to galactic winds (e.g. Rupke & Veilleux 2013a,b; Beirão et al. 2015; Leroy et al. 2015; Rupke, Gültekin & Veilleux 2017, and references therein).

6 SUMMARY

In this second paper of a series, deep *Herschel Space Observatory* data of six nearby dwarf galaxies selected to host known galactic-scale winds are used to investigate the structure and properties of the cold dust in and around these systems. Our analysis of these data has yielded the following results:

(i) The gain in both angular resolution and sensitivity of *Herschel* PACS and SPIRE over *Spitzer* MIPS has allowed us to detect and resolve previously unsuspected cold dust features in all six objects of our sample. These features have diverse morphologies: some are filamentary or clumpy, while others span a large range of galacto-centric angles. They extend out to 1–3 kpc, sometimes well beyond the stellar component. Some of these features coincide spatially with emission features in Hα, 8.0, and 24 μm data, but others do not.

(ii) We have used archival *Spitzer* 4.5 μm IRAC data to estimate the spatial extent of the stellar components in these objects and dis-

tinguish the dust emission that coincides with the 'disc' region, defined by this stellar component, from the emission that comes from the 'circumgalactic' region. We find that typically ∼10–20 per cent of the total dust mass resides in the circumgalactic region, reaching a value as large as ∼60 per cent in the case of NGC 1569. The presence of circumgalactic cold dust features in these dwarf galaxies does not obviously depend on the SFR surface density or gravitational influence of neighbouring galaxies, although the latter almost certainly plays a role in some objects (e.g. NGC 3077). The galaxy with the largest metallicity (O/H) deficit in our sample, NGC 1569, also happens to have the largest fraction of circumgalactic dust. This may be coincidental. The small number of galaxies in our sample and the substantial uncertainties on the measurements of the dust mass and gas metallicity preclude us from drawing any solid conclusion regarding a possible physical link between metallicity and circumgalactic dust mass fraction.

Our data do not allow us to determine unambiguously the origin of the circumgalactic dust. The best case in our sample for dust entrained in a galactic wind is NGC 1569, but we cannot rule out the possibility that cold dust features that appear to lie in the zone of influence of the galactic wind are instead dust features of external (e.g. tidal) origin in front or behind the wind. Future studies that not only consider the distribution of the circumgalactic dust with
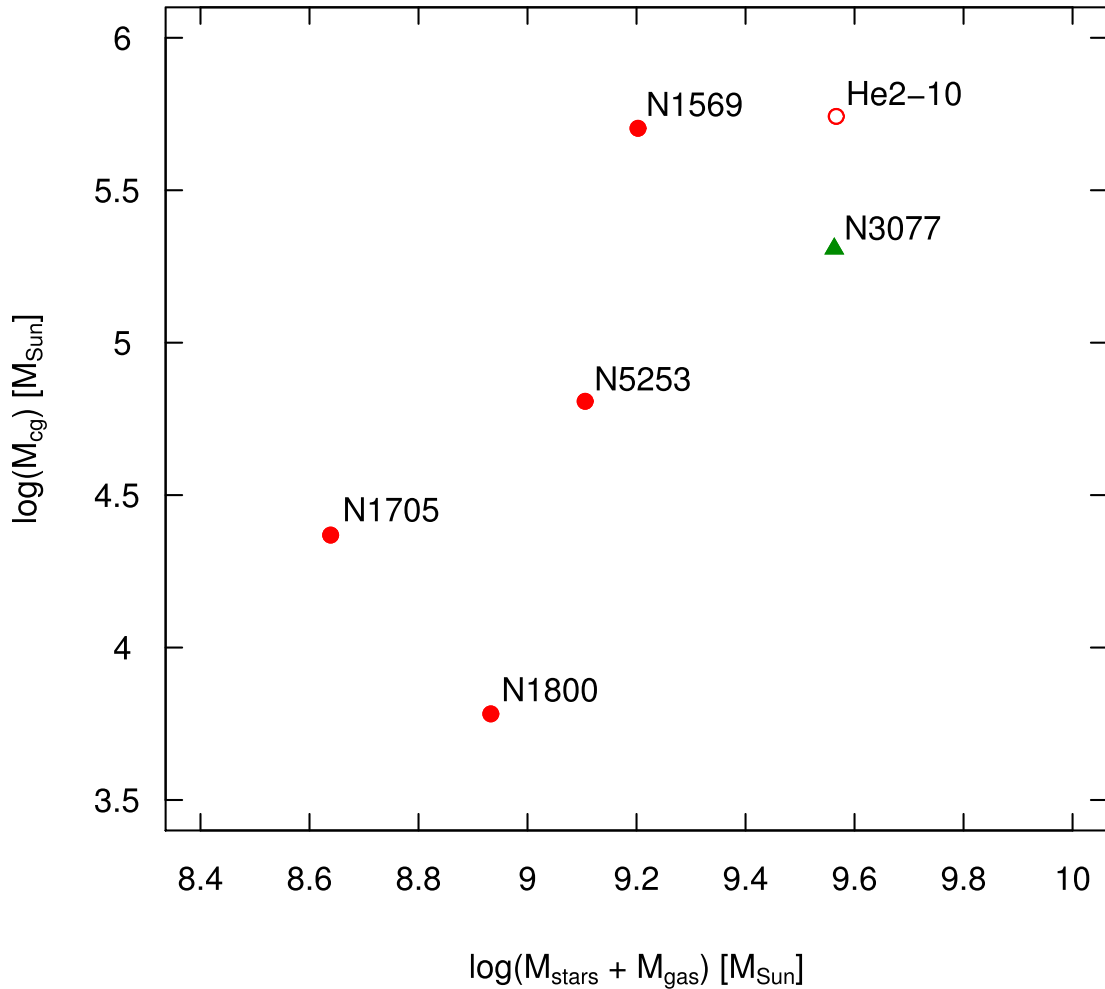
Figure 8. The circumgalactic dust mass is plotted against the total baryonic (stellar plus gas) mass, where the gas mass is the sum of the H I and H₂ gas masses. NGC 3077 is differentiated with a green triangle to indicate the likely tidal contribution to its circumgalactic dust features, and He 2–10 is differentiated with an open circle to indicate the possible AGN contribution to the FIR flux and therefore derived dust mass. With those caveats, this plot suggests a weak (Pearson's $r = 0.80$; P[null] 0.055) positive correlation between circumgalactic dust mass and total baryonic mass.

respect to the wind and tidal features but also the kinematics of dust tracers such H₂, CO, Na I D, and H I will help shed light on the origin of this far-flung dust in NGC 1569 and other dwarf galaxies.
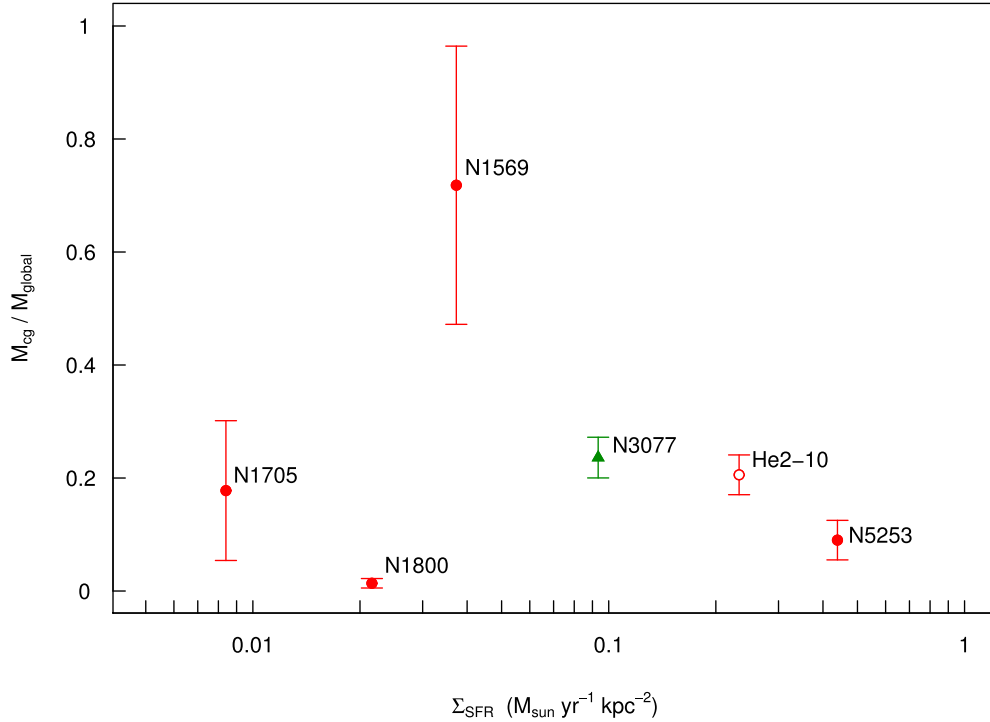
Figure 9. The circumgalactic dust mass fraction, M_{cg}/M_{global}, is plotted against the SFR surface density, Σ_{SFR} from Table 1. The uncertainty in M_{cg}/M_{global} comes from the uncertainties in the SED fitting (see Section 4.4 and Table 5). The meaning of the symbols is the same as in Fig. 8. No trend is seen in this figure between M_{cg}/M_{global} and Σ_{SFR}.
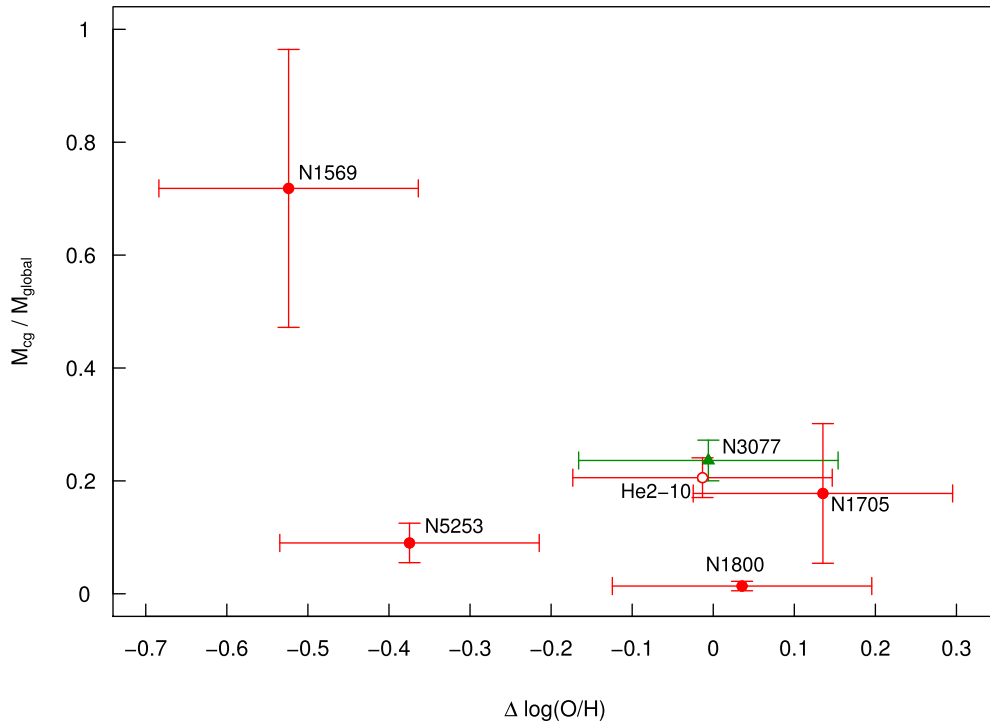

Figure 10. The circumgalactic dust mass fraction, M_{cg}/M_{global}, is plotted against the metallicity deficit, $\Delta \log(O/H)$, defined as the difference between the galaxy metallicity (see Table 1) and the metallicity predicted by the relation derived in Tremonti et al. (2004) between M_* and $12 + \log(O/H)$. The uncertainty on $\Delta \log(O/H)$ comes from the uncertainty in the galaxy metallicity ($\sim$0.1 dex) and the uncertainty in converting values to conform with Tremonti et al. (2004) ($\sim$0.06 dex). The meaning of the symbols is the same as in Fig. 8. No significant trend is seen in this figure between M_{cg}/M_{global} and $\Delta \log(O/H)$, although the object (NGC 1569) with the largest circumgalactic dust mass fraction also has the largest metallicity deficit.

(France); ASI (Italy); MCINN (Spain); SNSB (Sweden); STFC, UKSA (UK); and NASA (USA). HIPE is a joint development (are joint developments) by the Herschel Science Ground Segment Consortium, consisting of ESA, the NASA Herschel Science Center, and the HIFI, PACS, and SPIRE consortia.

REFERENCES

Aalto S., Garcia-Burillo S., Muller S., Winters J. M., van der Werf P., Henkel C., Costagliola F., Neri R., 2012, A&A, 537, A44

Alatalo K., 2015, ApJ, 801, L17

Alatalo K. et al., 2011, ApJ, 735, 88

Allende Prieto C., Lambert D. L., Asplund M., 2001, ApJ, 556, L63

Alton P. B., Davies J. I., Bianchi S., 1999, A&A, 343, 51

Aniano G., Draine B. T., Gordon K. D., Sandstrom K., 2011, PASP, 123, 1218

Ashley T., Elmegreen B. G., Johnson M., Nidever D. L., Simpson C. E., Pokhrel N. R., 2014, AJ, 148, 130

Balog Z. et al., 2014, Exp. Astron,, 37, 129

Banda-Barragán W., Federrath C., Crocker R., Bicknell G., 2016, MNRAS, 455, 1309

Barrera-Ballesteros J. K., Sánchez S. F., Heckman T., Blanc G. A., The MaNGA Team, 2017, ApJ, 844, 80

Beirão P., Armus L. et al., 2015, MNRAS, 451, 2640

Bell E. F., McIntosh D. H., Katz N., Weinberg M. D., 2003, ApJS, 149, 289

Bolatto A. D. et al., 2013, Nature, 499, 450

Brüggen M., Scannapieco E., 2016, ApJ, 822, 31

Calzetti D., Conselice C. J., Gallagher J. S., III, Kinney A. L., 1999, AJ, 118, 797

Calzetti D., Harris J., Gallagher J. S., III, Smith D. A. Conselice C. J., Homeier N., Kewley L., 2004, AJ, 127, 1405

Calzetti D. et al., 2010, ApJ, 714, 1256

Casey C. M., 2012, MNRAS, 425, 3094

Cicone C. et al., 2014, A&A, 562, AA21

Cooper J. L., Bicknell G. V., Sutherland R. S., Bland-Hawthorn J., 2008, ApJ, 674, 157

Cooper J. L., Bicknell G. V., Sutherland R. S., Bland-Hawthorn J., 2009, ApJ, 703, 330

Cottrell G. A., 1976, MNRAS, 174, 455

Curran S. J., Johansson L. E. B., Rydbeck G., Booth R. S., 1998, A&A, 338, 863

Dalcanton J. J. et al., 2009, ApJS, 183, 67

Dale D. A. et al., 2009, ApJ, 703, 517

Davé R., Rafieferantsoa M. H., Thompson R. J., Hopkins P. F., 2017, MNRAS, 467, 115

de Vaucouleurs G., de Vaucouleurs A., Corwin H. G., Jr., Buta R. J., Paturel G., Fouqué P., 1991, Third Reference Catalogue of Bright Galaxies. Springer, New York, NY (RC3)

della Ceca R., Griffiths R. E., Heckman T. M., MacKenty J. W., 1996, ApJ, 469, 662

Draine B. T., 2003, ARA&A, 41, 241

Draine B. T. et al., 2007, ApJ, 663, 866

Ehle M., Dahlem M., Jiménez Bailón E., Santos-Lleó M., Read A. M., 2004, in Duc P.-A., Braine J., Brinks E., eds, IAU Symp. 217, Recycling Intergalactic and Interstellar Medium, held in Syndey, Australia, Astron. Soc. Pac., San Francisco, p. 154

Engelbracht C. W. et al., 2006, ApJ, 642, L127

Erb D. K., Quider A. M., Henry A. L., Martin C. L., 2012, ApJ, 759, 26

Faucher-Giguère C.-A., Quataert E., 2012, MNRAS, 425, 605

Feldmann R., 2015, MNRAS, 449, 3274

Ferrara A., Scannapieco E., 2016, ApJ, 833, 46

Ferrarese L., Merritt D., 2000, ApJ, 539, L9

Feruglio C., Maiolino R., Piconcelli E., Menci N., Aussel H., Lamastra A., Fiore F., 2010, A&A, 518, L155

Feruglio C. et al., 2015, A&A, 583, A99

Fischer J. et al., 2010, A&A, 518, L41

Gebhardt K. et al., 2000, ApJ, 539, L13

Gnedin N. Y., Draine B. T., 2014, ApJ, 795, 37

Griffin M. J. et al., 2010, A&A, 518, L3

Grocholski A. J. et al., 2008, ApJ, 686, L79

Gültekin K. et al., 2009, ApJ, 698, 198

Heckman T. M., Armus L., Miley G. K., 1990, ApJS, 74, 833

Heckman T. M., Dahlem M., Lehnert M. D., Fabbiano G., Gilmore D., Waller W. H., 1995, ApJ, 448, 98

Heckman T. M., Lehnert M. D., Strickland D. K., Armus L., 2000, ApJS, 129, 493

Heckman T. M., Sembach K. R., Meurer G. R., Strickland D. K., Martin C. L., Calzetti D., Leitherer C., 2001, ApJ, 554, 1021

Högbom J. A., 1974, A&AS, 15, 417

Hunter D. A., 1996, ApJ, 457, 671

Hunter D. A., Hawley W. N., Gallagher J. S., III, 1993, AJ, 106, 1797

Hunter D. A., van Woerden H., Gallagher J. S., III, 1994, ApJS, 91, 79

Huo Z. Y., Xia X. Y., Xue S. J., Mao S., Deng Z. G., 2004, ApJ, 611, 208

Irwin J. A. et al., 2011, MNRAS, 410, 1423

Johnson M., 2013, AJ, 145, 146

Johnson K. E., Leitherer C., Vacca W. D., Conti P. S., 2000, AJ, 120, 1273

Johnson M., Hunter D. A., Oh S.-H., Zhang H.-X., Elmegreen B., Brinks E., Tollerud E., Herrmann K., 2012, AJ, 144, 152

Jurac S., Johnson R. E., Donn B., 1998, ApJ, 503, 247

Kaneda H., Yamagishi M., Suzuki T., Onaka T., 2009, ApJ, 698, L125

Kaneda H. et al., 2010, A&A, 514, A14

Karachentsev I. D., Makarov D. I., 1999, in Barnes J. E., Sanders D. B., eds, Proc. IAU Symp. Vol. 186, Galaxy Interactions at Low and High Redshift. Kluwer, Dordrecht, p. 109

Karachentsev I. D., Kaisina E. I., Makarov D. I., 2014, AJ, 147, 13

Kashino D., Renzini A., Silverman J. D., Daddi E., 2016, ApJ, 823, L24

Kennicutt R. C., Jr, Lee J. C., Funes S. J., José G., Sakai S., Akiyama S., 2008, ApJS, 178, 247

Kennicutt R. C., Jr et al., 2009, ApJ, 703, 1672

Kewley L. J., Ellison S. L., 2008, ApJ, 681, 1183

Kobulnicky H. A., Martin C. L., 2010, ApJ, 718, 724

Kobulnicky H. A., Skillman E. D., 2008, AJ, 135, 527

Kobulnicky H. A., Dickey J. M., Sargent A. I., Hogg D. E., Conti P. S., 1995, AJ, 110, 116

Kobulnicky H. A., Kennicutt R. C., Jr, Pizagno J. L., 1999, ApJ, 514, 544

Koribalski B. S. et al., 2004, AJ, 128, 16

Kormendy J., Ho L. C., 2013, ARA&A, 51, 511

Krügel E., 2002, Wiley Praxis Series in Astronomy and Astrophysics, Vol. 10. John Wiley & Sons Inc., Hoboken. NJ

Lara-López M. A., Bongiovanni A., Cepa J., Pérez García A. M., Sánchez-Portal M., Castañeda H. O., Fernández Lorenzo M., Pović M., 2010, A&A, 519, 31

Lehnert M. D., Heckman T. M., 1995, ApJS, 97, 89

Lequeux J., 2005, The Interstellar Medium, Translation from the French language edition of: Le Milieu Interstellaire by James Lequeux, EDP Sciences, 2003 Edited by J. Lequeux. Astronomy and Astrophysics Library. Springer, Berlin

Leroy A. K. et al., 2015, ApJ, 814, 83

Lindberg J. E. et al., 2016, A&A, 587, A15

Makovoz D., Khan I., 2005, in Shopbell P., Britton M., Ebert R., eds, ASP Conf. Ser. Vol. 347, Astronomical Data Analysis Software and Systems XIV. Astron. Soc. Pac., San Francisco, p. 81

Mannucci F., Cresci G., Maiolino R., Marconi A., Gnerucci A., 2010, MNRAS, 408, 2115

Marlowe A. T., Heckman T. M., Wyse R. F. G., Schommer R., 1995, ApJ, 438, 563

Martin C. L., 1997, ApJ, 491, 561

Martin C. L., 1998, ApJ, 506, 222

Martin C. L., 1999, ApJ, 513, 156

Martin C. L., 2005, ApJ, 621, 227

Martin C. L., Kennicutt R. C., Jr, 1995, ApJ, 447, 171

Martin C. L., Kobulnicky H. A., Heckman T. M., 2002, ApJ, 574, 663

Martin C. L., Shapley A. E., Coil A. L., Kornei K. A., Bundy K., Weiner B. J., Noeske K. G., Schiminovich D., 2012, ApJ, 760, 127

McCormick A., Veilleux S., Rupke D. S. N., 2013, ApJ, 774, 126

McCourt M., O'Leary R. M., Madigan A.-M., Quataert E., 2015, MNRAS, 449, 2

McDowell J. C. et al., 2003, ApJ, 591, 154

McQuade K., Calzetti D., Kinney A. L., 1995, ApJS, 97, 331

Meléndez M. et al., 2015, ApJ, 804, 46

Méndez D. I., Esteban C., Filipović M. D., Ehle M., Haberl F., Pietsch W., Haynes R. F., 1999, A&A, 349, 801

Meurer G. R., Freeman K. C., Dopita M. A., 1989, Ap&SS, 156, 141

Meurer G. R., Freeman K. C., Dopita M. A., Cacciari C., 1992, AJ, 103, 60

Meurer G. R., Staveley-Smith L., Killeen N. E. B., 1998, MNRAS, 300, 705

Moshir M. et al., 1990, BAAS, 22, 1325

Moustakas J., Kennicutt R. C., Jr, 2006, ApJS, 164, 81

Moustakas J., Kennicutt R. C., Jr, Tremonti C. A., Dale D. A., Smith J.-D. T., Calzetti D., 2010, ApJS, 190, 233

Muratov A., Kereš D., Faucher-Giguère C.-A., Hopkins P. F., Quataert E., Murray N., 2015, MNRAS, 454, 2691

Naab T., Ostriker J. P., 2017, ARA&A, 55, 59

Nims J., Quataert E., Faucher-Giguère C.-A., 2015, MNRAS, 447, 3612

Ott S., 2010, in Yoshihiko M., Koh-Ichiro M., Masatoshi O., eds, ASP Conf. Ser. Vol. 434, Astronomical Data Analysis Software and Systems XIX, Astron. Soc. Pac., San Francisco, p. 139

Ott J., Martin C. L., Walter F., 2003, ApJ, 594, 776

Paalvast M., Brinchmann J., 2017, MNRAS, 470, 1612

Pettini M., Pagel B. E. J., 2004, MNRAS, 348, L59

Pietsch W., Vogler A., Klein U., Zinnecker H., 2000, A&A, 360, 24

Pilbratt G. L. et al., 2010, A&A, 518, L1

Poglitsch A. et al., 2010, A&A, 518, L2

Radovich M., Kahanpää J., Lemke D., 2001, A&A, 377, 73

Rasmussen J., Stevens I. R., Ponman T. J., 2004, MNRAS, 354, 259

Reach W. T. et al., 2006, AJ, 131, 1479

Read A. M., Ponman T. J., Strickland D. K., 1997, MNRAS, 286, 626

Reines A. E., Sivakoff G. R., Johnson K. E., Brogan C. L., 2011, Nature, 470, 66

Reines A., Reynolds M. T., Miller J. M., Sivakoff G. R., Greene J. E., Hickox R. C., Johnson K. E., 2016, ApJ, 830, L35

Rémy-Ruyer A. et al., 2014, A&A, 563, A31

Rémy-Ruyer A. et al., 2015, A&A, 582, A121

Richings A. J., Faucher-Giguère C.-A., 2018, MNRAS, 474, 3673

Roussel H., 2013, PASP, 125, 1126

Roussel H. et al., 2010, A&A, 518, L66

Rupke D. S. N., Veilleux S., 2013, ApJ, 768, 75

Rupke D. S. N., Veilleux S., 2013, ApJ, 775, L15

Rupke D. S., Veilleux S., Sanders D. B., 2002, ApJ, 570, 588

Rupke D. S., Veilleux S., Sanders D. B., 2005a, ApJS, 160, 87

Rupke D. S., Veilleux S., Sanders D. B., 2005b, ApJS, 160, 115

Rupke D. S., Veilleux S., Sanders D. B., 2005c, ApJ, 632, 751

Rupke D. S. N., Gültekin K., Veilleux S., 2017, ApJ, 850, 40

Sakai S., Ferrarese L., Kennicutt R. C., Jr, Saha A., 2004, ApJ, 608, 42

Sakamoto K. et al., 2006, ApJ, 636, 685

Sánchez S. F. et al., 2017, MNRAS, 469, 2121

Sanders D. B., Mazzarella J. M., Kim D.-C., Surace J. A., Soifer B. T., 2003, AJ, 126, 1607

Scannapieco E., Brüggen M., 2015, ApJ, 805, 158

Schaye J. et al., 2015, MNRAS, 446, 521

Schwartz C. M., Martin C. L., 2004, ApJ, 610, 201

Shapley A., 2011, ARA&A, 49, 525

Skrutskie M. F. et al., 2003, yCat, 7233, 0

Smith M. W. L. et al., 2012, ApJ, 756, 40

Spitoni E., Calura F., Matteucci F., Recchi S., 2010, A&A, 514, A73

Steidel C. C., Erb D. K., Shapley A. E., Pettini M., Reddy N., Bogosavljević M., Rudie G. C., Rakic O., 2010, ApJ, 717, 289

Strickland D. K., Stevens I. R., 1999, MNRAS, 306, 43

Strickland D. K., Heckman T. M., Colbert E. J. M., Hoopes C. G., Weaver K. A., 2004a, ApJS, 151, 193

Strickland D. K., Heckman T. M., Colbert E. J. M., Hoopes C. G., Weaver K. A., 2004b, ApJ, 606, 829

Sturm E. et al., 2011, ApJ, 733, L16

Tacconi-Garman L. E., Sturm E., Lehnert M., Lutz D., Davies R. I., Moorwood A. F. M., 2005, A&A, 432, 91

Tanner R., Cecil G., Heitsch F., 2016, ApJ, 821, 7

Tanner R., Cecil G., Heitsch F., 2017, ApJ, 843, 137

Tassis K., Kravtsov A. V., Gnedin N. Y., 2008, ApJ, 672, 888

Telford O. G., Dalcanton J. J., Skillman E. D., Conroy C., 2016, ApJ, 827, 35

Thronson H. A., Jr, Wilton C., Ksir A., 1991, MNRAS, 252, 543

Tosi M., Sabbi E., Bellazzini M., Aloisi A., Greggio L., Leitherer C., Montegriffo P., 2001, AJ, 122, 1271

Tremonti C. A. et al., 2004, ApJ, 613, 898

Tully R. B., 1988, Nearby Galaxies Catalog. Cambridge Univ. Press, Cambridge

van der Hulst J. M., 1979, A&A, 75, 97

Veilleux S., Cecil G., Bland-Hawthorn J., 2005, ARA&A, 43, 769

Veilleux S., Rupke D. S. N., Swaters R., 2009, ApJ, 700, L149

Veilleux S. et al., 2013, ApJ, 776, 27

Veilleux S. et al., 2017, ApJ, 843, 18

Vogelsberger M. et al., 2014, MNRAS, 444, 1518

Waller W. H., 1991, ApJ, 370, 144

Walter F., Heithausen A., 1999, ApJ, 519, L69

Walter F., Weiss A., Scoville N., 2002, ApJ, 580, L21

Walter F., Brinks E., de Blok W. J. G., Bigiel F., Kennicutt R. C., Jr, Thornley M. D., Leroy A., 2008, AJ, 136, 2563

Walter F. et al., 2011, ApJ, 726, L11

Weiner B. J. et al., 2009, ApJ, 692, 187

Westmoquette M. S., Smith L. J., Gallagher J. S., 2008, MNRAS, 383, 864

Young J. S. et al., 1995, ApJS, 98, 219

Yun M. S., Ho P. T. P., Lo K. Y., 1994, Nature, 372, 530

Zahid H. J., Bresolin F., Kewley L. J., Coil A. L., Davé R., 2012, ApJ, 750, 120

Zastrow J., Oey M. S., Veilleux S., McDonald M., Martin C. L., 2011, ApJ, 741, L17

Zastrow J., Oey M. S., Veilleux S., McDonald M., 2013, ApJ, 779, 76

Zubovas K., King A. R., 2014, MNRAS, 439, 400

Zubovas K., Nayakshin S., Sazonov S., Sunyaev R., 2013, MNRAS, 431, 793

APPENDIX A: NOTES ON INDIVIDUAL GALAXIES

For the discussion in these notes, please refer to Figs 1(a)–(f) and Figs 2(a)–(f).

(i) *He 2-10*: broad cold dust emission regions surround He 2–10 out to ~1.5 kpc in all SPIRE bands as well as the 160 μm PACS map. The 160 μm emission map appears similar in extent and morphology to the H I distribution observed by Kobulnicky et al. (1995). The 70 μm PACS map exhibits a bit more anisotropy in its distribution of circumgalactic emission with tapering features extending to the north–northeast, southwest, and east-southeast. The north–northeast feature extends furthest to ~2.6 kpc. The orientation of these tapering features appears similar to the smaller 0.5 kpc-scale Hα bubbles (Méndez et al. 1999; Zastrow et al. 2013), but appears less correlated with the shape of the X-ray emission (Kobulnicky & Martin 2010). Several knots of emission separated from He 2–10 by ~3–4 kpc to the north-west and southwest in the PACS maps cannot be definitively ruled out as background sources given the signal-to-noise levels or foreground Milky Way dust clouds, but coincident emission in the SPIRE maps seems connected to the disc via colder streams bridging their separation. The most prominent emission in the SPIRE maps towards the knots north-west of the disc seems

similarly oriented to an X-ray feature observed by Kobulnicky & Martin ([2010](#)).

(ii) *NGC 1569*: a dense complex of filamentary and broad circumgalactic cold dust features stretch out from all along the disc of NGC 1569. The prominent Hα, 8.0, and 24 μm filament (Waller [1991](#); Hunter et al. [1993](#); Westmoquette et al. [2008](#); McCormick et al. [2013](#)) extending southwest from the western edge of the disc also shows up in the PACS maps, but becomes fainter and disappears in the SPIRE bands. A clump of cold dust directly south of the galactic nucleus resides ∼1.8 kpc from the disc mid-plane and appears to have made a clean break with the other circumgalactic cold dust emission in the PACS maps. Some faint 8.0 μm emission (McCormick et al. [2013](#)) coincides with this rogue clump and some extended X-ray emission (Heckman et al. [1995](#); della Ceca et al. [1996](#)) may as well. The rogue clump has no obvious counterpart in Hα emission, but supershell features surrounding its location (Martin [1998](#); Westmoquette et al. [2008](#)) suggest that it resides at the centre of an ionized gas shell. The structure of the rogue clump suggests anisotropic heating with the warmer 70 μm emission closer to the galactic disc and the colder emission in the SPIRE maps extending further away. The bright emission to the southwest corner of the SPIRE maps comes from foreground Milky Way cirrus, although emission from dust possibly associated with the large-scale H I complex studied by Johnson et al. ([2012](#)) and Johnson ([2013](#)) cannot be ruled out. Note that some dispute remains about the distance to NGC 1569 (Grocholski et al. [2008](#)). We have adopted the distance determined by Grocholski et al. ([2008](#)), which employs *Hubble Space Telescope* data and the tip of the red giant branch to obtain a redshift-independent distance of 3.36 Mpc, but the range of published distance measurements (1.9–3.4 Mpc) leads to a broad range of SFRs.

(iii) *NGC 1705*: vertical filamentary cold dust emission to the north and south of NGC 1705 coincides with the H I emission, which Meurer et al. ([1998](#)) have shown consists mainly of a rotating disc. However, Meurer et al. also note an H I 'spur' which is kinematically distinct from the rotating disc and spatially consistent with the Hα outflow (Meurer et al. [1989](#), [1992](#); Zastrow et al. [2013](#)). Our PACS maps show evidence of a similarly consistent cold dust feature extending almost exactly north from the galaxy. Also in the PACS maps, two bright knots of emission directly to the south are separated from the galactic centre by ∼1.3 and 1.5 kpc, respectively. These knots are also approximately coincident with the rotating H I disc, also appear in the SPIRE maps, and do not have associated background sources. North–northeast of the nucleus, a bright cloud of cold dust appears as a knot in the 70 μm PACS map but has broader spatial extent in our other four *Herschel* maps. This cloud with no obviously associated background source seems spatially consistent with the orientation of the northern Hα superbubble (Zastrow et al. [2013](#)), but resides well beyond its edge (>0.5 kpc), making it a likely example of material swept out of the ISM by an expanding superbubble. However, we did not include this cloud in the global flux measurements, since it cannot be definitively ruled out as a background source.

(iv) *NGC 1800*: a C-shaped filament of circumgalactic cold dust extends from the northwestern edge of NGC 1800 to ∼1.2 kpc north of the disc in the 70 μm PACS map tracing a similar feature in 8.0 μm emission. In addition there is some more diffuse, less bright 70 μm emission above the disc to the east of this filament. These features lie just south of the filamentary web of Hα emission (Hunter, van Woerden & Gallagher [1994](#); Marlowe et al. [1995](#); Hunter [1996](#)). The cold dust features along the northwestern edge of NGC 1800 are offset from the Hα 'fingers' of Hunter ([1996](#)),

which extend from the northeastern edge of the disc. An offset also exists between the southern edge cold dust features which appear like two broad nubs splayed out from the eastern and western edges of the disc in our SPIRE maps versus the centrally concentrated Hα 'fingers' and shell outside the disc (again from Hunter [1996](#)). Observations by Rasmussen et al. ([2004](#)) reveal X-ray emission crossing the disc of NGC 1800 approximately from southeast to north-west at an angle with respect to the stellar component. The northern extent of this hot X-ray gas above the disc appears to coincide with some of the emission from cold dust in the PACS maps. Within the galactic disc, the peak of the dust emission is offset to the west from the stellar component, perhaps helping explain why the strongest dust feature − the C-shaped filament extending north − emanates from that part of galaxy. This offset between dust and stellar emission might be explained by ram pressure stripping, but the galaxy appears to be relatively isolated (Karachentsev et al. [2014](#)). What may appear as cold dust knots to the south in the PACS images could also be either Galactic dust heated by foreground Milky Way stars or emission from background sources evident in the 4.5 μm IRAC map.

(v) *NGC 3077*: most if not all of the circumgalactic cold dust features we observe for NGC 3077 can be attributed to the same tidal interaction forces with M81 and M82, which produce tidal arms of H I and the complex of H I and CO offset to the east of the galaxy's stellar component (Cottrell [1976](#); van der Hulst [1979](#); Yun et al. [1994](#); Walter & Heithausen [1999](#)). However, certain cold dust features appear to complement the morphology of the Hα emission (Martin [1998](#); Calzetti et al. [2004](#)). A C-shaped filament and a knot of cold dust at its tip extending ∼2.6 kpc north of the stellar disc (see 70 and 160 μm maps) reside directly above the location of an Hα shell (Calzetti et al. [2004](#)). A circumferential arc of cold dust visible in the PACS maps and the 250 μm SPIRE map to the south of the disc also traces the edge of a superbubble observed in Hα and X-ray emission (Martin [1998](#); Ott et al. [2003](#)). Cold dust filaments, clouds, broad regions, and clumps to the east and west of NGC 3077 are likely associated with the H I features (Yun et al. [1994](#); Walter et al. [2011](#)). The argument has been made that the superbubbles of hot plasma and ionized gas have yet to break out of this galaxy but potentially have enough energy to generate a breakout wind in the northern direction where there is less H I density (Ott et al. [2003](#)). The cold dust emission along the north–south direction in the PACS maps appears stronger than the east–west emission, while the inverse is true of the east–west emission in the SPIRE maps, which would seem to support the argument for a wind developing in the northern direction. Our deep PACS data provide evidence for this north–south emission, which was not identified in a previous analysis of the SPIRE data (Walter et al. [2011](#)).

(vi) *NGC 5253*: the morphology of the circumgalactic cold dust features in our PACS and SPIRE maps appears to follow the distribution of H I (Kobulnicky & Skillman [2008](#)) more closely than any other galaxy component. However, features like the broad emission regions extending from the north-west and southeast edges of the stellar disc in the *Herschel* maps do follow ionized gas features (Marlowe et al. [1995](#); Calzetti et al. [1999](#); Zastrow et al. [2011](#)), X-ray emission (Martin & Kennicutt [1995](#); Strickland & Stevens [1999](#)), and some 8.0 μm features (McCormick et al. [2013](#)). Filaments extend south in the 70, 160, and 250 μm maps, where the westernmost filament protruding from the southwest edge of the disc extends at least ∼2 kpc from the disc. In the PACS maps, a circumgalactic cold dust filament also extends directly north from the disc. Looking along the north–south direction, the 500 μm SPIRE map shows tenuous evidence for a significantly larger scale bipolar

filamentary emission extending to ∼5 kpc outside the galactic disc. The southern extent of this emission appears disturbed and perhaps coincides with the H I plume interpreted by Kobulnicky & Skillman (2008) as a potential outflow or inflow. However, no obvious counterpart for the northern filament presents itself in the H I images. The challenge of ruling out background sources or cold Milky Way dust clouds remains a concern for this north–south emission, but the brightest features from apparent clouds within this structure are >4σ above the background in the 500 μm SPIRE map.

This paper has been typeset from a TEX/LATEX file prepared by the author.